Geologica Acta, Vol.15, Nº 4, December 2017, 283-304, I-VII
DOI: 10.1344/GeologicaActa2017.15.4.3

geologica acta

Petrology and geochronology of the Porriño late-Variscan pluton from NW Iberia. A model for post-tectonic plutons in collisional settings

L. GONZÁLEZ-MENÉNDEZ[1] G. GALLASTEGUI[1] A. CUESTA[2] P. MONTERO[3] A. RUBIO-ORDÓÑEZ[2] J.F. MOLINA[3] F. BEA[3]

[1]Instituto Geológico y Minero de España (IGME)
Avda. Real 1, 24006, León, Spain. González-Menéndez E-mail: l.gonzalez@igme.es; Tel.:+34 987262171
Matemático Pedrayes 25, 33005, Oviedo, Spain. Gallastegui E-mail: g.gallastegui@igme.es

[2]Department of Geology, University of Oviedo
C/ Jesús Arias de Velasco s/n, 33005 Oviedo, Spain. Cuesta E-mail: acuesta@geol.uniovi.es
Rubio-Ordóñez E-mail: arubio@geol.uniovi.es

[3]Department of Mineralogy and Petrology, University of Granada, Campus Fuentenueva
18002, Granada, Spain. Montero E-mail: pmontero@ugr.es. Molina E-mail: j.f.molina@ugr.es;
Bea E-mail: fbea@ugr.es

ABSTRACT

The Variscan orogen of NW Iberia contains abundant syn- and post-tectonic granitoids. The post-tectonic granitoids are metaluminous to slightly peraluminous, I-type granites, monzogranites ± granodiorites ± tonalites. The Porriño pluton studied here is a representative example. It consists of two units: i) a pink-red, peraluminous, biotite granite and ii) a gray, metaluminous to peraluminous, biotite (± amphibole ± titanite) monzogranite, including mafic-intermediate enclaves. SHRIMP U-Pb dating yielded 290-295Ma ages for all the units. The mineralogy and geochemistry show that the pink-red granite has features of I- and A-type granites, whereas the gray monzogranite and enclaves are I-types. Sr isotopes show scattered values for the pink-red granite ($^{87}Sr/^{86}Sr_{295Ma} \approx 0.702$-$0.710$) and uniform values for the gray monzogranite and enclaves ($^{87}Sr/^{86}Sr_{295Ma} \approx 0.705$-$0.706$). Geochemical results indicate a peritectic entrainment of clinopyroxene + orthopyroxene ± Ca-plagioclase ± ilmenite ± garnet, and minor accessory phases (± zircon ± titanite ± apatite) into a melt similar to the leucocratic gray monzogranite. A mafic-intermediate source is proposed for the gray monzogranite and its enclaves. Restitic protoliths generated granitic melts with A-type features such as the pink-red granite. The I-type nature of many post-tectonic granitoids could be explained by the previous extraction of S-type syn-tectonic granites that left restites and less fertile rocks. Late orogenic new melting affected the previously unmelted and more mafic lithologies of the lower-middle crust, and gave rise to I-type granitoids. Repeated melting events affecting such lithologies and previous restites could have generated granitic melts with A-type features.

KEYWORDS | **Post-orogenic magmatism. Variscan orogeny. Post-tectonic granites. Monzogranites. Enclaves.**

INTRODUCTION

The study of granitoids from continental orogens is a way to unravel the processes of internal geochemical differentiation operating in the continental crust during mountain range formation. Mountain belts such as the Himalayas, the Andes, the Urals, and the eroded Variscan chain are field laboratories to investigate the granitic magmatism linked to orogeny. Among these belts, the Variscan orogen offers a widespread amount of syn- and post-tectonic granitoids emplaced at middle-upper crustal levels (~ 5-15km depth), the space-temporal distribution of which can be precisely related to the deformational phases of the Variscan orogeny (Bea, 2004; Cuesta and Gallastegui, 2004).

Post-tectonic granitoid intrusions related to orogenic belts have been an important focus of research (Turner *et al.*, 1992; Roberts and Clemens, 1993; Bea *et al.*, 1994; King *et al.*, 1997; Debon and Lemmet, 1999; Bonin, 2004; Villaseca *et al.*, 2009). The preservation of their original magmatic features (mineralogy, textures, geochemistry and isotope geochemistry) permits a better understanding of the petrogenetic processes compared with syn-tectonic granitoids. In the Variscan orogenic belt, as well as in other orogens, post-tectonic granitoids constitute an important volume of igneous rocks related to orogenic processes and frequently they include different types of ores.

Post-tectonic granitoids are commonly formed by granodiorites, granites and leucogranites with minor tonalites, diorites and gabbros. The granite-granodiorites are usually I- or A-type (Bonin, 2004) although in some orogens they can be S-type, as in some parts of the Variscan belt (Bea, 2004; Merino Martínez *et al.*, 2014) and the Himalaya (Sylvester, 1998). Post-tectonic granitoids of high K, calc-alkaline composition have been interpreted as markers of past subduction/arc settings and mantle derivation (Finger and Steyer, 1990; Kemp *et al.*, 2007; Castro, 2013) but some authors argue that the only requirement for the generation of such granitoids is an appropriate calc-alkaline mafic to intermediate lower crustal source (Roberts and Clemens, 1993; Villaseca *et al.*, 2009; Clemens *et al.*, 2011). The difficulties of melting experiments to generate granodiorites ± monzogranites, similar to the Iberian post-tectonic granitoids, led to some authors (*e.g.* Castro *et al.*, 1999) to propose a mixing-assimilation process between mantle mafic melts and gneisses.

Post-tectonic granitoids are interpreted to set, in some cases, the time when the crust is stabilized after an orogenic event (Elliot, 2003). Time constrains based on numerical modeling indicate that melting events linked to orogenic processes occur 20-50Ma after crustal thickening due to accumulation of radiogenic heat (England and Thompson, 1986; Thompson and Connolly, 1995; Bea *et al.*, 2003; Bea, 2012). In the Iberian Variscan orogen, the difference in age between the tectonic thickening (347-354Ma, Rubio Pascual *et al.*, 2013) and many syn-tectonic granitoids (≈ 320Ma) is 27-34Ma, a gap in agreement with the models (Bea, 2012). On the other hand, post-tectonic magmatism in the northwestern Iberian Massif (≈ 290-300Ma) has a 47-54Ma gap with the tectonic thickening. In this view, syn-tectonic granitoids could be related to the previous thickening events when the orogenic belt was in its main constructive stage. This helps to explain its abundant occurrence in the internal orogenic domains, where the crust has been considerably thickened. Post-tectonic granitoids probably had another melting mechanism.

Post-tectonic granitoids are interpreted by some authors (Turner *et al.*, 1992; Altherr *et al.*, 2000; Kemp *et al.*, 2007) as magmatic intrusions linked to post-orogenic processes such as lithospheric delamination and asthenospheric mantle uplifts (and/or post-orogenic mantle melt intrusions into the crust) that promoted crustal melting and post-tectonic granitoid intrusions. Such processes link the petrogenesis of post-tectonic I-type granitoids to the anorogenic bimodal magmatic suites (commonly of A-type nature), thus explaining their similarities in some cases (Whalen *et al.*, 1987; Chappell and White, 1992; Turner *et al.*, 1992; King *et al.*, 1997; Fernández-Suárez *et al.*, 2000; Bonin, 2004; Pérez-Soba and Villaseca, 2010). In the Iberian Variscan belt, a variation of this model of granitoid generation and its relationship with the coeval generation of the late-Variscan Ibero-armorican arc has been proposed (Gutiérrez-Alonso *et al.*, 2004, 2011).

Post-tectonic granitoids are abundant in the hinterland orogenic zones of the NW Iberian Variscan belt while its abundance decreases towards the external orogenic zones. A representative example in the NW Iberia Variscan belt is the Porriño pluton (Fig. 1), which is related to ore mineralizations of Au-Ag and sulfides (Fe, Mo, Sb), and has been widely used as a building and ornamental stone, especially its pink-red facies.

Here we present an integrated study of the petrology, geochemistry and U-Pb SHRIMP geochronology aimed to explain a genetic model for the Porriño granitoid useful for similar post-tectonic granitoids of NW Iberia and other similar orogenic settings. We will try to explain the origin of the granitic units of the pluton, the differences and similarities with other granitoids in the Iberian Variscan massif and contribute to the debate of mantle *vs.* crustal origin, in terms of melting heat and source rocks for this type of granitoid magmatism.

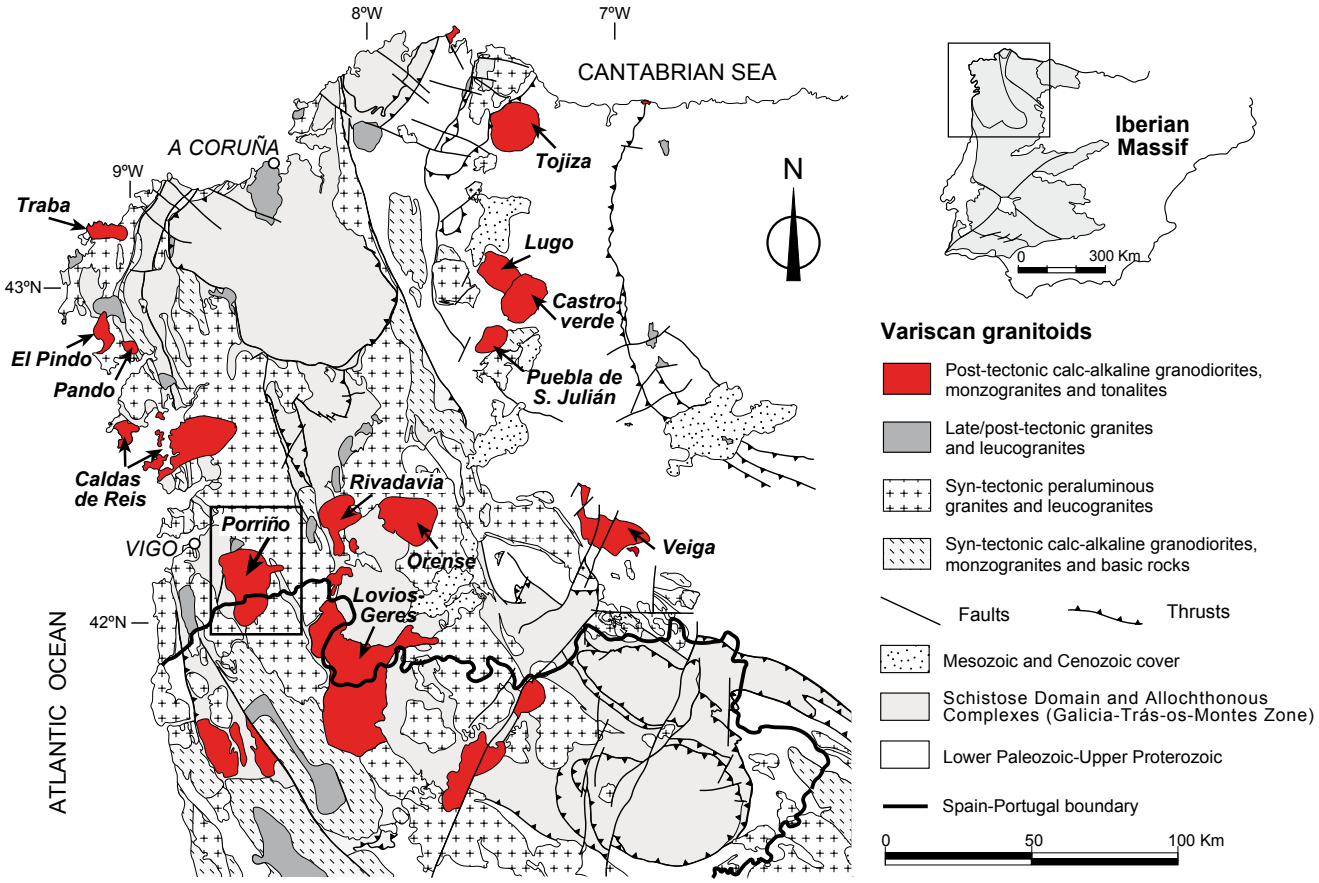

FIGURE 1. Sketch of the Iberian massif and simplified geological map of the NW Variscan granitoids showing the location of the Porriño pluton (modified from Dallmeyer *et al.*, 1997, and Cuesta and Gallastegui, 2004).

GEOLOGICAL SETTING

Variscan granites in NW Iberia

The northwest Iberian massif is composed of Late Proterozoic and Early Paleozoic metasediments, granitoids and felsic volcanics, variably metamorphosed, ophiolite/island arc allocthonous complexes and abundant Variscan granitoids. The most intense Variscan orogenic events took place between ~360Ma and 290Ma and produced: i) Crustal thickening, high P metamorphism and emplacement of allochthonous complexes and parautochthonous units, and ii) low to locally high grade metamorphism and widespread granitic magmatism (*e.g.* Pérez-Estaún and Bea, 2004). After the original classifications of Capdevila and Floor (1970) and Capdevila *et al.* (1973), the main types of Variscan granitoids in the NW Iberian massif were defined as: i) syn-tectonic metaluminous/peraluminous tonalite-granodiorite intrusions, ii) syn-tectonic peraluminous granites, iii) late-tectonic peraluminous granites and iv) post-tectonic metaluminous-peraluminous granites-granodiorites (Corretgé *et al.*, 2004; Cuesta and Gallastegui, 2004). This sequence of granitoid intrusions is characterized by an alternation of S- and I-type magma generation and can be grouped in two events of high granitoid production: i) An initial S-type predominant syn-tectonic magmatism (≈ 315-325Ma, ≈ 320Ma average; this event also includes less abundant I-type, calc-alkaline rocks); ii) A later I-type predominant, post-tectonic magmatism (≈ 290-300Ma; this event also includes a small volume of S-type granitoids).

Post-tectonic Variscan granitoids of the NW Iberian Variscan massif (Fig. 1) are intruded into previously deformed, metamorphosed schists and granitoids (from previous magmatic stages). Their shapes are varied but often are rounded to elliptical. Magnetic fabric and structural surveys in some of these bodies suggest small thickness and elongated shapes in 3D with relatively narrow roots (Yenes *et al.*, 1999; Aranguren *et al.*, 2000). The granitoids are composed of a range of different igneous lithologies. In some cases, a single pluton can show a wide range of igneous compositions

(Caldas de Reis pluton, Cuesta, 1991; Lovios-Gerês massif, Cottard, 1979; Barrera Morate *et al.*, 1989; Mendes and Dias, 2004), whereas in other cases it can be composed of just one, apparently homogeneous, unit (La Tojiza and Lugo-Castroverde plutons, Bellido Mulas *et al.*, 1987).

The Porriño post-tectonic pluton

The Porriño pluton (Corretgé *et al.*, 1981; Bellido *et al.*, 2005; Villaseca *et al.*, 2009; Simões *et al.*, 2013) is emplaced at epizonal crustal levels (≈ 2.5-3.5kbar). It consists of i) a pink-reddish ± equigranular coarse grained granite in the western part of the pluton, ii) a gray ± porphyritic coarse grained monzogranite that occupies most of the pluton outcrop, and iii) small sized mafic-intermediate bodies hosted by the gray monzogranite and showing evidence of mixing/reaction with its host thus suggesting that both magmas (enclave and gray monzogranite) were contemporaneous (Fig. 2). The gray monzogranite is cut, in some outcrops, by dykes (1-3m thick) of fine grained biotite granite. The contacts among the different units can be either sharp or transitional.

At the outcrop scale, the Porriño granites are isotropic. Only in very few outcrops feldspar phenocrysts show a slight N-S, or NW-SE orientation. Analyses of magnetic susceptibility from Simões *et al.* (2013) show low magnetic anisotropy and subhorizontal magnetic foliations and lineations.

SAMPLES AND METHODOLOGY

We worked with 14 representative samples from the Porriño pluton (Fig. 2). All of them were studied under the optical microscope. A subset of 13 samples were analyzed for major and trace elements, a subset of 7 samples were also analyzed for Sr and Nd, and zircon concentrates were extracted from 4 samples. All these analyses and the trace-element composition of minerals from 4 samples were performed at the Scientific Analytical Centre (CIC, Centro de Instrumentación Científica) of the University of Granada (Spain). Major-element compositions of minerals from 7 samples were determined at the Technical-Scientific Services of the University of Oviedo (Spain).

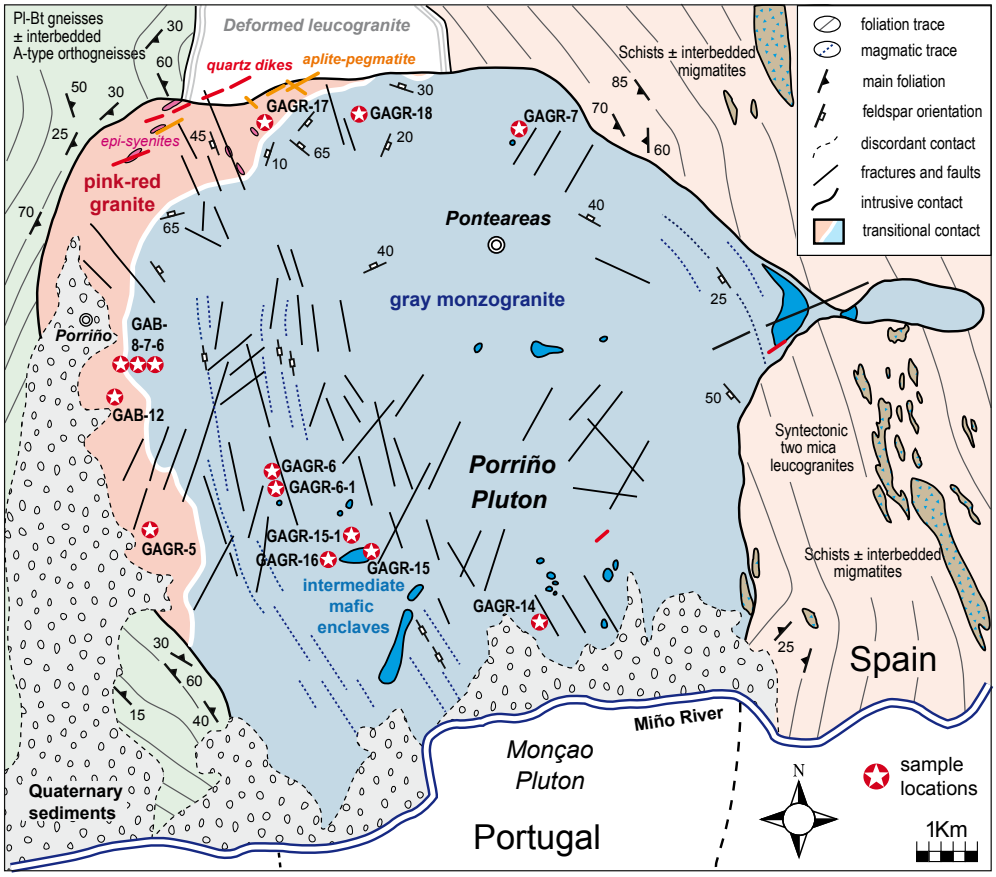

FIGURE 2. Modified geological map (after Corretgé *et al.*, 1981 and Barrera Morate *et al.*, 1989) of the post-tectonic Variscan Porriño pluton, including field observations and sample locations.

Whole-rock major-element and Zr determinations were performed by X-ray fluorescence after fusion with lithium tetraborate. Typical precision was better than ±1.5% for an analyte concentration of 10 wt.%, and ±2.5% for 100ppm Zr. Trace elements were determined by ICP-MS after HNO_3 + HF digestion of 0.1000g of sample powder in a Teflon-lined vessel at 180°C and 200psi for 30min, evaporation to dryness, and subsequent dissolution in 100ml of 4 vol.% HNO_3; the precision was better than ±5% for analyte concentrations of 10ppm. The concentration of Hf was calculated from the ICPMS-determined Zr/Hf and the XRF-determined Zr concentration. Samples for Sr and Nd isotope analyses were digested with HNO_3+HF using ultra-clean reagents and analyzed by thermal ionization mass spectrometry (TIMS) in a Finnigan Mat 262 spectrometer after chromatographic separation with ion-exchange resins. Normalization values were $^{86}Sr/^{88}Sr = 0.1194$ and $^{146}Nd/^{144}Nd = 0.7219$. Blanks were 0.6 and 0.09ng for Sr and Nd respectively. The external precision (2σ), estimated by analyzing 10 replicates of the standard WS–E (Govindaraju *et al*., 1994) was better than ±0.003% for $^{87}Sr/^{86}Sr$ and ±0.0015% for $^{143}Nd/^{144}Nd$. $^{87}Sr/^{86}Rb$ and $^{143}Sm/^{144}Nd$ were directly determined by ICP-MS following the method developed by Montero and Bea (1998), with a precision better than ±1.2% and ±0.9% (2σ), respectively.

Major-element compositions of minerals were determined by electron microprobe using a Camebax SX-100 (CAMECA) with a voltage intensity of 15kv, current of 15nA, and acquisition time of 10s per element. A combination of silicates and oxides was used for calibration. The quality of results was improved by using the Bureau de Recherches Geologiques et Minières (BRGM) standards. Analyses of a secondary standard as an unknown under the same conditions as sample measurement suggested an accuracy of 1%.

Trace-element composition of minerals were determined by LA-ICP-MS using a 213nm Mercantek Nd-YAG laser coupled to an Agilent 7500 ICP-MS with a shielded plasma torch. The ablation was carried out in a He atmosphere using a laser beam fixed at 80–95 microns diameter. The spot was pre-ablated for 45s using a laser repetition rate of 10Hz and 40% output energy. Afterwards, the spot was ablated for 60s at 10Hz with a laser output energy of 75%. In order to minimize mass fractionation and to increase sensitivity (Bea *et al*., 1996), an active focus mode was used (Hirata and Nesbitt, 1995), setting the stage to move 5lm every 20s NIST-610 glass (*ca*. 450ppb of each element) was employed as an external standard. In each analytical session of a single thick section, the NIST- 610 glass was analyzed at the beginning and at the end, and also after every 9 spots to correct for drift. Concentration values were corrected using silicon as an internal standard. Data reduction was carried out in STATA programming language (Statacorp, 2005). The precision, calculated on 5 to 7 replicates of the NIST-610 glass measured in every session, was in the range ±3 to ±7% for most elements. Further details on technical methods can be found in Bea (1996) and Bea *et al*. (2005).

Zircon was separated by panning, first in water and then in ethanol. The concentrate was purified by hand picking. About one hundred zircon grains of each sample, plus several grains of standards were cast on a 3.5cm diameter epoxi mount, polished and documented using optical and scanning electron microscopy. After extensive cleaning and drying, mounts were coated with ultra-pure gold (8–10nm thick) and inserted into the SHRIMP for analysis. Each selected spot was rastered with the primary beam for 120s prior to the analysis, and then analyzed 6 scans, following the isotope Peak sequence $^{196}Zr_2O$, ^{204}Pb, $^{204.1}$background, ^{206}Pb, ^{207}Pb, ^{208}Pb, ^{238}U, ^{248}ThO, ^{254}UO. Every mass in scans was measured sequentially 10 times with the following total counting times per scan: 2s for mass 196; 5s for masses 238, 248, and 254; 15s for masses 204, 206, and 208; and 20s for mass 207. The primary beam, composed of $^{16}O^{16}O^+$, was set to an intensity of about 5nA, with a 120μm Kohler aperture, which generated 17 x 20 micron elliptical spots on the target. The secondary beam exit slit was fixed at 80μm, achieving a resolution of about 5000 at 1% peak height.

All calibration procedures were performed on the standards included on the same mount. Mass calibration was done on the REG zircon (*ca*. 2.5Ga, very high U, Th, and common lead content). Every analytical session started measuring the SL13 zircon, which was used as a concentration standard (238ppm U). The TEMORA-2 zircon (416.8 ± 1.1Ma, Black *et al*., 2003), used as isotope ratios standard, was then measured every 4 unknowns.

RESULTS

Petrography

The pink-red granite

This coarse-grained granite shows a seriate to equigranular texture with K-feldspar as the abundant phase. The granite is composed of quartz (23-30%), K-feldspar (45-52%), plagioclase (16-20% and An^{26-13}) and biotite (3-6%). The main accessory minerals are allanite (Fig. 3D), zircon, apatite and scarce ilmenite. In the Q-A-P modal diagram it plots as a syenogranite/

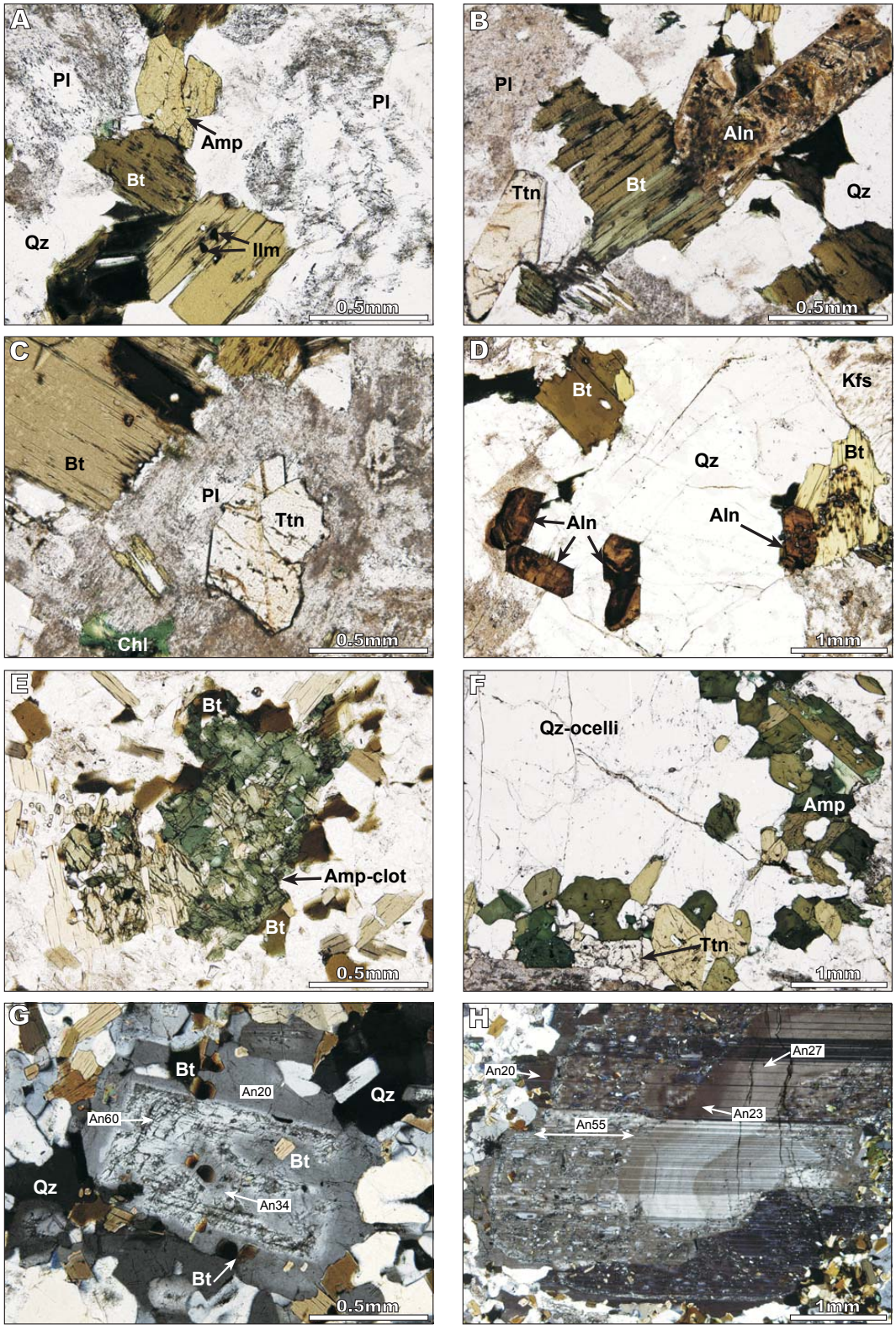

FIGURE 3. Photomicrographs. A) Plagioclase (Pl), quartz (Qz), subhedral amphibole (Amp) and biotite (Bt) including subrounded ilmenite (Ilm) in the gray monzogranite. B) Rhythmic zoned allanite (Aln) and titanite (Ttn) in the gray monzogranite. C) Titanite and chlorite (Chl) included within plagioclase in the gray monzogranite. D) Rhythmic zoned allanite, biotite and K-feldspar (Kfs) in the pink-red granite. E) Amphibole clot, probably pseudomorph after clinopyroxene, in microgranular enclave. F) Partial view of large quartz ocelli with amphibole + titanite rim in mafic enclave. G) Ca-rich plagioclase partially corroded and mantled by Na-rich plagioclase in microgranular enclave. H) Large plagioclase crystal with Na-rich zoned core, Ca-rich mottled zone and Na-rich external rim in microgranular enclave. (A-F, plane polarized light; G and H, crossed polars).

quartz-syenite. Plagioclase and quartz show similar sizes and textural features as those of the gray monzogranite.

The perthitic K-feldspar crystals are pink-red, thus giving the unit its distinguishing color. These K-feldspar crystals are more abundant and contain more inclusions (H_2O-fluid, iron oxides, alteration products, etc.) compared to those of the gray monzogranite. Biotite appears as single crystals or forming clots with big crystals of zoned allanite (≈ 1-2mm) in either case mainly occupy grain boundaries. Opaque minerals (ilmenite) are rare and occur only associated with biotite.

The gray monzogranite

This is a coarse grained granite and has a seriate to porhyritic texture formed of K-feldspar phenocrysts. The major mineral phases are quartz (29-37%), plagioclase (33-36% and An^{41-25}), K-feldspar (20-30%), biotite (4-13%), amphibole (0.5-1.5%) and titanite (<1%). The main accessory minerals are allanite, zircon, apatite and scarce ilmenite. Using the Q-A-P modal proportions (quartz-K-feldspar-plagioclase), this unit can be classified as a monzogranite/granodiorite.

Quartz crystals show a range of sizes (≈ 0.1-0.5cm). Plagioclase forms euhedral crystals of smaller size and is frequently altered. K-feldspar appears mainly as large euhedral phenocrysts (≈ 0.5-3cm). Biotite appears as single crystals or forming clots. Amphibole can appear as single subhedral crystals (Fig. 3A), as polycrystalline aggregates or clots (± titanite ± biotite), and as inclusions in plagioclase and K-feldspar. The very irregular shapes of some amphibole grains might indicate partial dissolution processes. Titanite (Fig. 3B; C) occurs as a late crystallization phase occupying the inter-granular spaces between quartz and feldspars, as isolated idiomorphic crystals included in feldspars, or partially included in amphibole (forming clots, with or without biotite). Secondary or subsolidus titanite is rare.

Allanite crystals are quite abundant in some samples, reaching similar modal proportions to titanite. Crystals have maximum sizes between 1 and 3mm and show distinctive zonation patterns (Fig. 3B). Scarce and tiny fluorite crystals appear either interleaved with biotite or included in plagioclase; their textural relations suggest a secondary origin. Other minor secondary phases are chlorite, epidote and sericite in plagioclase cores. Garnet is present in fine-grained granite dykes crosscutting the gray monzogranite.

Mafic-intermediate enclaves

The gray monzogranite hosts abundant enclaves of quartz-diorites, quartz-monzodiorites, tonalites, and granodiorites. The enclaves often show a porphyritic texture with plagioclase phenocrysts (part of them may be xenocrysts), quartz ocelli, amphibole clots and less K-feldspar. The fine-grained matrix is formed by quartz, plagioclase, biotite, amphibole, ± K-feldspar, titanite, ilmenite, zircon and needle-like apatite. The fine grain size and the abundance of needle-like apatite indicate quenching of enclave magma against the cooler host granitoid. Magmatic orientations defined by plagioclase, biotite and amphibole crystals occur. Amphibole appears either as single crystals, as clots (up to 3mm in size) surrounded by biotite (Fig. 3E), as rims bordering quartz ocelli (Fig. 3F) and as inclusions within Ca-rich plagioclase. Amphibole-biotite clots could be pseudomorphs after anhydrous mafic phases (clinopyroxene) or after peritectic phases from the melting stages, nevertheless none of these possible phases were identified. However, clinopyroxene partially replaced by amphibole ± biotite clots is frequent in tonalites and mafic microgranular enclaves in the similar Caldas de Reis pluton (Cuesta, 1991).

Mineral chemistry

Major element chemistry of the main minerals

Representative electron microprobe analyses of plagioclase, amphibole and biotite are presented in Table I (ELECTRONIC APPENDIX I, available at www.geologica-acta.com).

Plagioclase crystals of the two granites show oscillatory zoning with alternate bands of An^{29} and An^{11} with outer rims of albite. However, the gray monzogranite has plagioclase crystals with cores richer in anorthite, up to An^{46-41}. Plagioclase from the mafic-intermediate enclaves is sharply different. Most crystals are euhedral, formed by a nearly uniform core with An^{60-53} and sharp outer rims of An^{20-17}. The most calcic cores show different degrees of dissolution/resorption and are preserved as corroded crystals mantled by An^{34-20} plagioclase (Fig. 3G). These could represent partially resorbed restitic or peritectic plagioclase (Clemens and Bezuidenhout, 2014). Large plagioclase crystals (≈ 1cm) show oscillatory zoned cores of An^{27-23} and outer rims of An^{20}, separated by a mottled zone of An^{60-55} (Fig. 3H). These large plagioclases were probably incorporated from the gray monzogranite (xenocrysts) and reacted with the mafic magma providing evidence of mixing between coeval magmas.

Amphibole is calcic, with Fe/(Fe+Mg)= 0.56-0.76, low TiO_2 (0.4-1.8%) and low $Fe^{3+}/(Fe^{3+}+Fe^{2+})$ ratio (0.10-0.21). Based on Leake *et al.* (1997) classification, subhedral dark-green amphibole is hastingsite and ferro-edenite, while that in polycrystalline clots is ferro-hornblende. The amphibole in microgranular enclaves (mme) has a remarkable variation

in Fe/(Fe+Mg) ratio (0.56-0.76) and Al^{IV} (0.68-1.79 a.p.f.u.); the lower values correspond to amphibole clots. In mafic-intermediate enclaves and gray monzogranite the Fe/(Fe+Mg) ratio is close to the range 0.68-0.74 (Fig. 4A). Amphiboles with high Fe/(Fe+Mg) and low $Fe^{3+}/(Fe^{3+}+Fe^{2+})$ crystallize at low-fO_2 (Czamanske *et al.*, 1981; Anderson and Smith, 1995). In the Porriño pluton amphibole crystallized at moderate-fO_2 conditions compared to those in oxidized and reduced A-type granites (Anderson and Smith, 1995; Dall'Agnol *et al.*, 2005) (Fig. 4A).

Biotite has similar TiO_2, Al_2O_3, MnO, Na_2O and K_2O in all rock types but in the pink-red granite it exhibits lower MgO (2.6-3.4%), high FeO_t (29.3-32.5%), and very high FeO_t/MgO (8.9-12.0) compared to the gray monzogranite and enclaves (MgO: 5.1-7.9%; FeO_t: 22.5-29.1%; FeO_t/MgO: 3.1-5.1). The Fe/(Fe+Mg) value of biotite in the gray monzogranite and enclaves is 0.64-0.76, similar to the coexisting amphibole (Fig. 4A; B). The lowest Fe/(Fe+Mg) corresponds to biotite from microgranular enclaves (mme) (0.64-068), while in mafic-intermedite enclaves and gray monzogranite this relation is 0.70-0.76. In the pink-red granite, biotite Fe/(Fe+Mg) shows higher values (0.83-0.87) being constant with increasing Al^{IV} (Fig. 4B). According to the Fe/(Fe+Mg) ratio, biotite from microgranular enclaves plots in the magnetite granitoid field whereas biotite from the granites and mafic-intermediate enclaves plots in the ilmenite-granitoid field

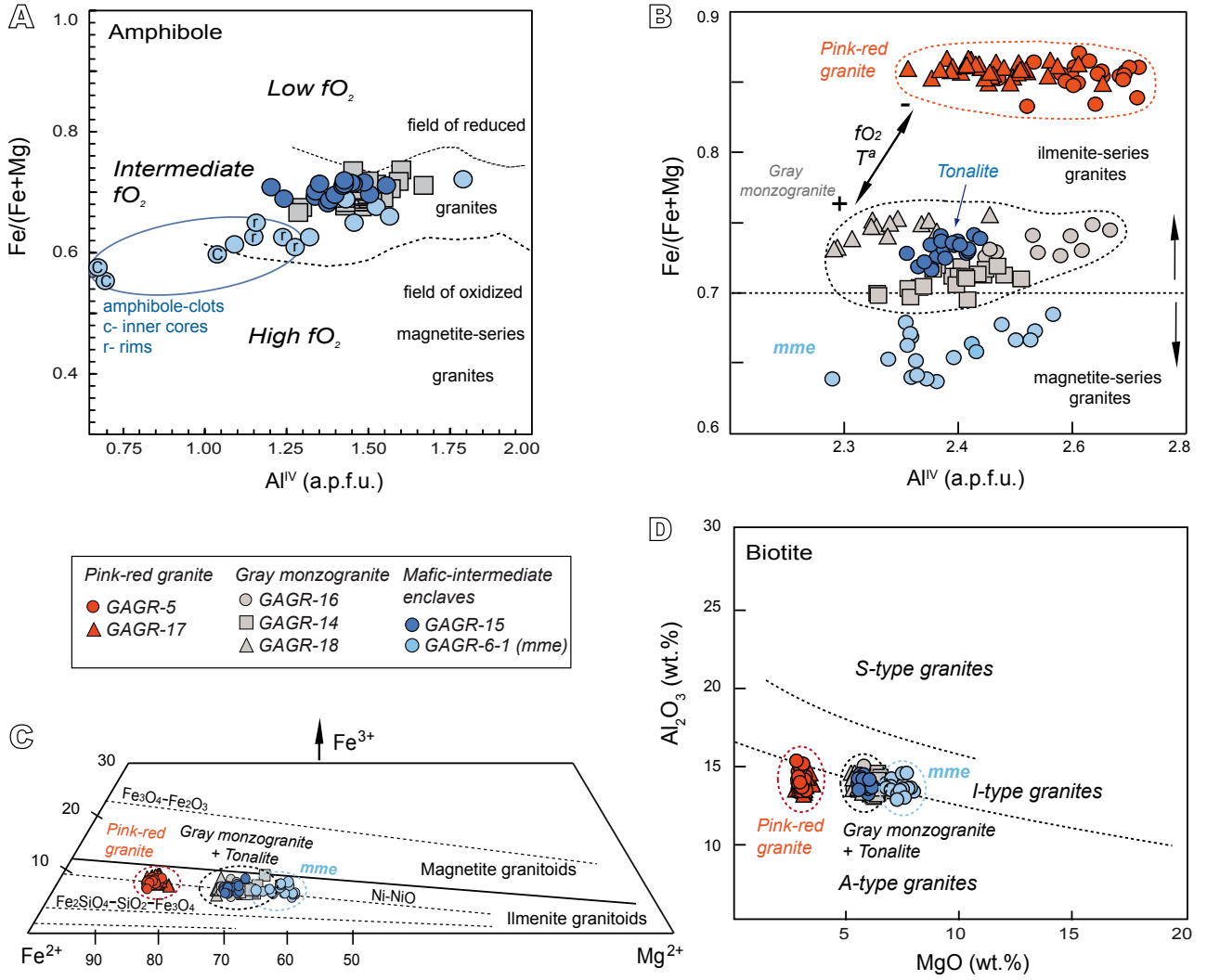

FIGURE 4. Amphibole and biotite compositions in the granitoid units and mafic-intermediate enclaves of the Porriño pluton. A) Amphibole plot in the Fe/(Fe+Mg) *vs.* Al^{IV} diagram. Dashed lines based on hornblende composition in oxidized and reduced anorogenic granites (Anderson and Smith, 1995). B) Biotite composition in the Fe/(Fe+Mg) *vs.* Al^{IV} diagram. Fields of magnetite and ilmenite granites from Dall'Agnol *et al.* (2005). C) Fe^{3+}-Fe^{2+}-Mg diagram for biotites; dashed lines correspond to compositions of "buffered" biotites (Wones and Eugster, 1965). D) Biotite plot in the Al_2O_3 *vs.* MgO discrimination diagram from Villaseca *et al.* (2009).

(Dall'Agnol *et al.*, 2005). However, all biotites have low $Fe^{3+}/(Fe^{3+}+Fe^{2+})$ oxidation state (0.10-0.16; Fe^{3+} estimated from Bruiyn *et al.*, 1983) and fall on the Ni-NiO buffer (Wones and Eugster, 1965) reflecting reducing conditions during crystallization (Fig. 4C).

Because of the low Al_2O_3 and high FeO_t, biotite in the Porriño pluton have alkaline affinity but do not show a decrease in Al_2O_3 with increasing FeO_t as in alkaline granites (Abdel-Rahman, 1994). F content (F = 0.2-0.8%) also differs from that of alkaline granites (F > 1.5%; Anderson, 1983). In the $MgO-Al_2O_3$ diagram (Villaseca *et al.*, 2009) biotite of the gray monzogranite and related enclaves lies between the I- and A-type granite fields, whereas in the pink-red granite it plots in the A-type field (Fig. 4D).

In summary, the occurrence of Fe-rich biotite and amphibole, the low oxidation state of both minerals and the presence of ilmenite as the main oxide phase indicate that the Porriño pluton crystallized at fairly reducing conditions. Furthermore, the Fe/(Fe+Mg) suggests (Wones and Eugster, 1965) that in the pink-red granite, biotite crystallized at lower fO_2 and lower TºC than in the gray monzogranite and its related enclaves, a situation also described in the nearby post-tectonic Caldas de Reis pluton (Cuesta, 1991).

Trace element and REE chemistry

The composition of biotite shows slight differences between the main granites (Table II, ELECTRONIC APPENDIX I). The biotite from the pink-red granite is more homogeneous and despite some overlap, compared to the gray monzogranite, it has higher Nb (215ppm *vs.* 82ppm, average values) and Zn (784ppm *vs.* 500ppm), but lower Li (928ppm *vs.*1038ppm) and Ba (346ppm *vs.* 1186ppm). Compared to biotite from S-type granites in the southern Iberian Variscan massif (González-Menéndez, 1998), biotite from the Porriño pluton is lower in Li while the rest of the trace elements overlap considerably. Plagioclase compositions of the two granites are not so contrasting, but still some differences occur: pink-red granite plagioclase has higher Rb (4.5ppm *vs.* 2ppm) but lower Ba (30ppm *vs.* 104ppm) and Sr (40ppm *vs.* 265ppm). In the same way, K-feldspar from the pink-red granite has higher Rb (397ppm *vs.* 344ppm) but lower Sr (52ppm *vs.* 98ppm) than its analogues in the gray monzogranite. The amphibole from the gray monzogranite shows high contents in Y (315-322ppm), Zr (155-158ppm), Zn (447-462ppm), and low content in Ba (38-54ppm), Sr (22ppm) and Eu (4.5ppm). The total REE content of this amphibole (≈ 950-1000ppm) is similar or even higher than that of other major minerals that account for part of REE budget in crustal rocks, such as garnet (Bea, 1996). Chondrite-normalized pattern shows a small enrichment in MREE, Eu negative anomaly, and $(La/_NYb_N)\approx 2$.

Geochemistry

Table III (ELECTRONIC APPENDIX I) shows whole-rock major and trace element content from the different granitoid units of the Porriño pluton.

The gray monzogranite, compared to the pink-red granite, has lower content of SiO_2 (~69-73 wt.% *vs.* 71-76 wt.%), K_2O (~4.1-5.4 wt.% *vs.* 4.6-5.8 wt.%) and ASI values (0.98-1.03 *vs.* 1.03-1.12) but higher CaO (1.3-2 wt.% *vs.* 0.65-1.31 wt.%), MgO (~0.3-0.6 wt.% *vs.* 0.04-0.4 wt.%) and Na_2O (2.79-3.9 wt.% *vs.* 2.5-3.6 wt.%).

The other major elements occur in similar concentration in both granites (Al_2O_3: 12-15 wt.%, TiO_2: 0.1-0.44 wt.%, Fe_2O_3: 1.4-3.6 wt.%, P_2O_5: 0.03-0.14 wt.%) with slightly higher Al_2O_3 and TiO_2 in the gray monzogranite. Harker plots do not show significant differences between the two granites (Fig. 5) except for CaO and $Fe_2O_3{}^t$ which have distinct parallel trends for each granite. $Fe_2O_3/(Fe_2O_3+MgO)$ ratios show lower values for the gray monzogranite and higher ferroan values (A-type granitoid values) for the pink-red granite samples.

Trace element compositions of Porriño granites also overlap considerably but some significant differences may be recognized (Fig. 6). Most of them decrease with the B parameter (B= mol. Fe + Mg + Ti). The gray monzogranite, compared to the pink-red granite, has lower contents of Zr (155ppm *vs.* 169ppm, average) and LREE. On the contrary, it has more Sr (106ppm *vs.* 39ppm, average), V (24ppm *vs.* 10ppm) and HREE. The La/Lu ratio remains constant compared to B parameter in the gray monzogranite, while it increases markedly in the pink-red granite. Regarding the Zr content and the Ga/Al ratios both the gray monzogranite and the pink-red granite have values in the boundary between I/S and A-type granites (Fig. 6). Chondrite-normalized diagrams reveal that the gray monzogranite has lower Gd/Yb ratio thus causing a much flatter HREE normalized pattern than the pink-red granite (Fig. 7). The negative Eu anomaly is more pronounced in the pink-red granite. The REE pattern of one of the mafic enclaves (a quartz-monzodiorite) differs substantially from the two main granites. It has lower total REE, a flat HREE normalized pattern, and a smaller Eu negative anomaly.

Geochronology

Previous ages of the Porriño pluton consist of a K-Ar biotite age of 292Ma (Ries, 1979), a Rb-Sr age of 287±9Ma (gray monzogranite; García Garzón, 1987) and a recent

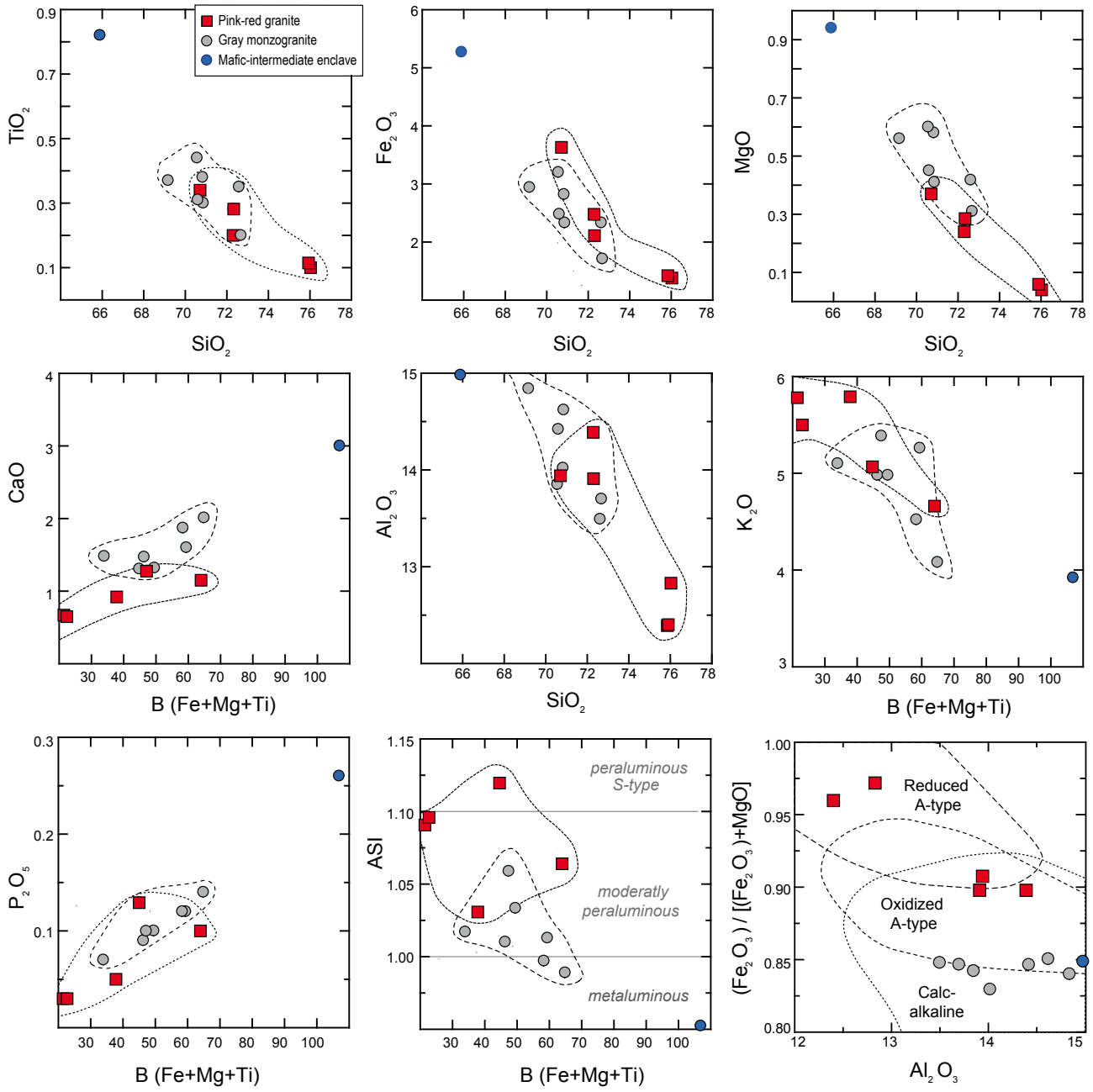

FIGURE 5. Geochemical variation diagrams for the major elements of the different granitoid units from the Porriño pluton. Both SiO_2 and the B parameter (Fe+Mg+Ti, in molar proportions) are used as differentiation indexes. ASI is the alumina saturation index (or A/CNK): $Al_2O_3/CaO+Na_2O+K_2O$) in molar proportions. Fields in the last diagram after Dall'Agnol and Oliveira (2007).

U-Pb SHRIMP age of 296±3Ma (Simões *et al.*, 2013). In the present work, U-Pb SHRIMP geochronology permits us to precisely date the different granitoid units of the Porriño pluton. U content in the studied zircons is exceptionally high (commonly ≈ 0.5-1 wt.%). This elevated U content caused the metamictization of the zircons and possible loose of radiogenic Pb. These features make them difficult to date and, consequently, a considerable amount of zircon crystals had to be analyzed.

Pink-red granite GAB-8. Zircons are euhedral, medium to short prismatic crystals with very short pyramidal terminations and an average maximum length from 150 to 250µm. Crystals are usually translucent light yellow or colorless and a few are opaque dark brown in color.

Most zircons are low cathodoluminescent and have a complex internal structure showing: i) abundant crystals

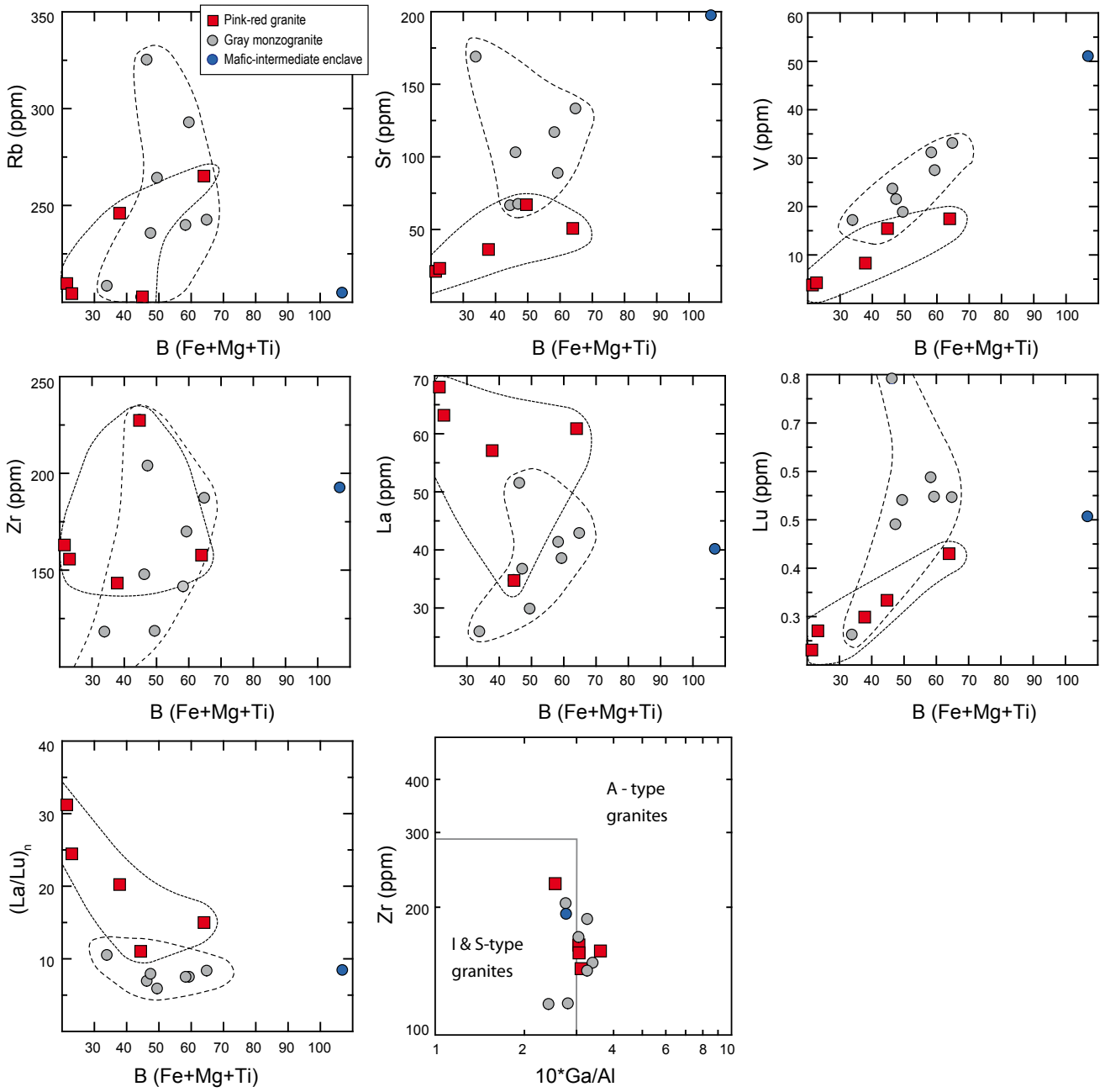

FIGURE 6. Variation diagrams for trace and rare earth elements of the granitoid units from the Porriño pluton. The B parameter (Fe+Mg+Ti, in molar proportions) is used as the differentiation index. Boundaries in the 10*Ga/Al *vs.* Zr diagram are after Whalen *et al.* (1987).

formed by gray cores with well defined oscillatory zoning, rimmed by very dark or black structureless overgrowths, ii) gray dark morphologically uniform crystals with diffuse zoning, iii) rare entirely black crystals with no internal structure and iv) a few crystal show a dark core surrounded by lighter rims (Fig. 8A). U content is variable but usually very high, with a maximum of *ca.* 4500ppm and an average of 1350ppm and an average Th/U ratio = 0.28 (Table IV, ELECTRONIC APPENDIX I).

Forty analyses were done in thirty-seven crystals, performed in rims and cores of all type of zircons. Half of the analyses are quite or very discordant, mainly due to a variable high proportion of uncorrectable common lead. After rejecting analyses with a discordance higher than 5%, eighteen of them cluster in the concordia yielding a $^{206}Pb/^{238}U$ age = 294 ± 1.5Ma (MSWD= 0.3) and a $^{207}Pb/^{235}U$ age = 297 ± 2.5Ma (MSWD = 0.6) (Fig. 8B; Table IV). According to the obtained ages, black overgrowths and lighter cores have the same age

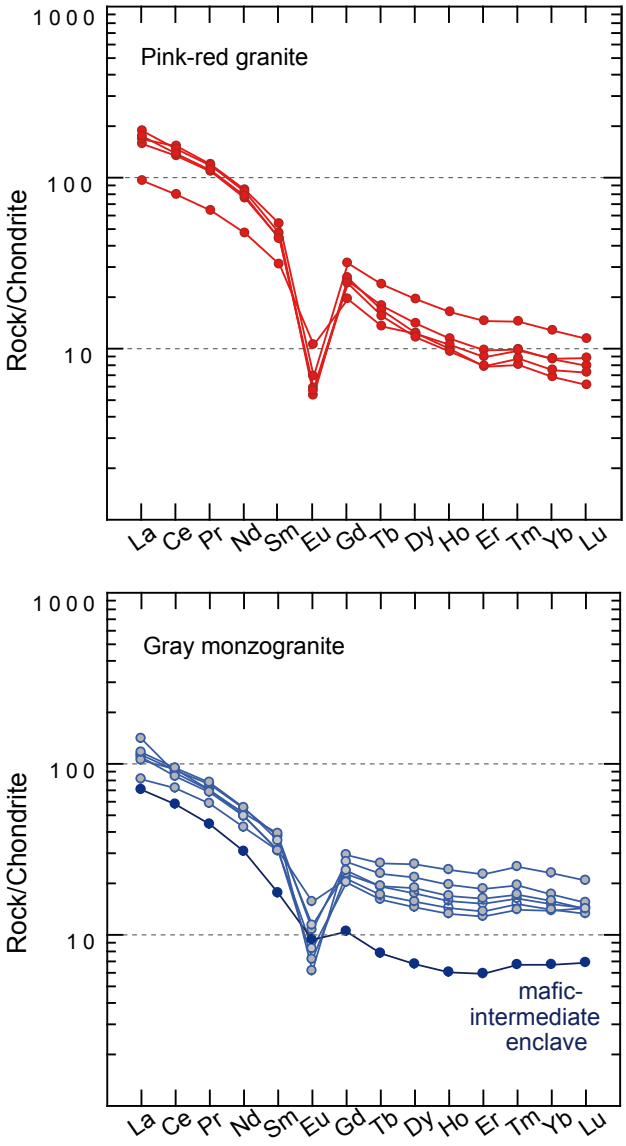

FIGURE 7. Rare Earth element diagrams normalized to chondrites (Nakamura, 1974) of the granitoid units from the Porriño pluton.

and were, therefore, formed during the same magmatic event.

Pink-red granite GAGR-5. Most zircons are euhedral, medium to short prismatic or stubby with short pyramidal terminations. Crystals are usually brown opaque and rarely translucent light brown or yellowish. Crystal sizes are variable, from 100 to >300µm in length and 50 to 150µm in thickness. Cathodoluminiscence images are complex and three types of internal morphologies can be described. Type 1 consists of a few crystals highly cathodoluminiscent with very light gray color in the internal parts and darker gray color in the outer ones, all of them record a well defined oscillatory and patchy zoning and rarely show a black or very dark rim (Fig. 8A). Type 2 crystals are more abundant and usually smaller than type 1. They show a dark gray internal part with oscillatory zoning and thick black rims with no internal structure (Fig. 8A). Type 3 crystals are abundant and have variable size; all of them are very low cathodoluminiscent or black and they never display internal structure. For U-Th-Pb analyses, we selected type 1 and type 2 zircons mainly, due to the high U content in type 3. The average U and Th content and the average Th/U ratio in analyzed zircons are 365ppm, 200ppm and 0.28, respectively (Table IV).

Thirty three analyses were performed in 32 crystals, most of them concordant or nearly concordant. After rejecting those with discordance >5%, we obtained a set of twenty two, which plot in the concordia in a unique cluster yielding a $^{206}Pb/^{238}U$ weighted age of 294 ± 3Ma (MSWD=3.3) and a $^{207}Pb/^{235}U$ weighted age = 292 ± 4Ma (MSWD=3.3) (Fig. 8C; Table IV).

Gray monzogranite GAB-6. Zircons are large (from 150 to more than 300µm as average length size), euhedral medium to long prismatic, rarely acicular and never rounded. They are usually translucent dark brown or yellow in color and a few are pale yellow or colorless.

Cathodoluminiscence images show very dark crystals, usually with gray and badly defined oscillatory zoned cores surrounded by thick black or very dark structureless rims, (Fig. 8A) growing concordantly or discordantly over the cores or even invading them. Zircons frequently present small cracks and inclusions.

Forty three U-Pb analyses were made in 30 grains. Analyses were performed in morphologically uniform zircons and core/rim pairs of morphologically complex crystals. Several analyses have moderate to high proportion of common lead so they are quite or very discordant. Ten other analyses also had a lead-loss combined with common-lead discordance and were rejected. The rest of discordant analyses define a 204-corrected discordia line yielding a lower intercept of 295 ± 3.6 with a MSWD = 2.3 (Fig. 8D; Table IV).

After common-lead 204-correction, 20 analyses had a discordance less than 5% [Discordance= 100*($^{207}Pb/^{235}U$ age-$^{206}Pb/^{238}U$ age)/($^{207}Pb/^{235}U$ age)]. Accordingly, they were the only ones used for mean age calculation.

Plotted in a Wetherill diagram, 19 concordant analyses cluster at $^{206}Pb/^{238}U_{(204\text{-corrected})}$ weighted age of 294 ± 4Ma with a MSWD = 2.6 perfectly matching the lower Intercept age (Fig. 8E). Their analyses plot after common lead correction at 717 ± 11Ma. These analyses correspond to a gray unzoned restitic core, morphological identical to the rest of cores, always younger.

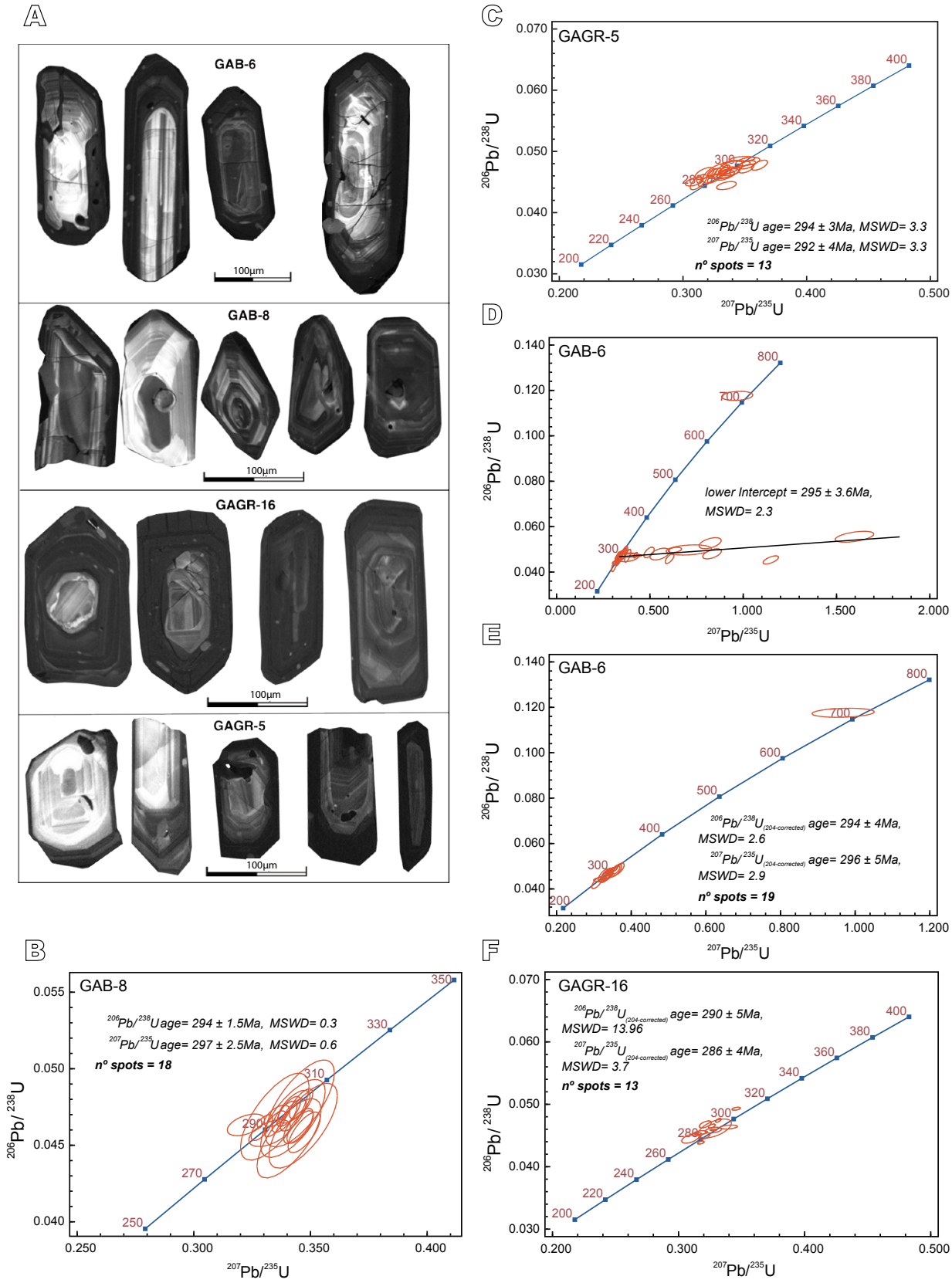

FIGURE 8. A) Cathodoluminiscence images of selected zircon grains from the pink-red granite (GAB-8, GAGR-5) and gray monzogranite (GAB-6, GAGR-16) of the Porriño pluton. Wetherill concordia plots: B) Pink-red granite GAB-8. C) Pink-red granite GAGR-5. D) and E) Gray monzogranite GAB-6. F) Gray monzogranite GAGR-16.

U, Th and Pb contents are large, particularly U, which can contain up to 6000ppm, with an average = 1960ppm and an average Th/U ratio = 0.19. In spite of the complex cathodoluminescent images showing well developed low cathodoluminescent rims (high U content) and higher cathodoluminescent cores, all yielded, except in one inherited grain, the same age (Table IV).

Gray monzogranite GAGR-16. Zircons are euhedral, medium prismatic with very short or non-existent pyramidal terminations. Less abundant are long prismatic to acicular crystals. Most are opaque dark brown and a few are translucent light brown to yellow. Average size is 150-250µm in length.

In all cases, zircons are extremely low cathodoluminescent, entirely black or formed by a dark gray core with a diffuse zonation surrounded by thick black structureless rims (Fig. 8A). U content is very high, with an average of >2300ppm and an average Th/U ratio of 0.2 (Table IV).

Forty nine analyses were performed in very low cathodoluminescent rims, in higher cathodoluminescent cores and in entirely black zircons (forty five crystals). In general zircons present a variable but usually high proportion of common lead, which makes most of the zircons to be quite or highly discordant. Common lead correction methods did not work properly for most of the cases, so for age calculation we used those analyses with less than 10% of discordance and then corrected for common lead using the 204-correction method. We obtained a cluster of thirteen analyses which yields a $^{206}Pb/^{238}U_{(204\text{-corrected})}$ weighted age of 290±5Ma (MSWD=13.9) and a $^{207}Pb/^{235}U_{(204\text{-corrected})}$ weighted age =286 ± 4Ma (MSWD=3.7). (Fig. 8F; Table IV).

As in previous samples, very different morphological areas of the zircons, as rims and cores, yielded the same age, thus reflecting that there was a unique magmatic episode but the U content in the magma or the U-partition for zircon changed during the crystallization stage.

In summary, both the pink-red granite and the gray monzogranite have similar U-Pb ages of 294Ma except for sample GAGR-16 of the gray monzogranite (290±5Ma) (Fig. 8F). Nevertheless we consider that all these ages are within the same error range and thus could correspond to a single magmatic event. This would support a contemporaneous intrusion and emplacement of the two main granite units (pink-red granite and gray monzogranite).

DISCUSSION

Magmatic differentiation processes

The main granitoid units of the Porriño pluton do not seem to be related to a common differentiation process. The different trends of CaO, Fe_2O_3, Sr, V and REE between the two granitoids (Figs. 5 and 6) preclude sequential crystallization or magma mixing, in which the more mafic terms should lie in continuity with the more felsic ones.

The differences in REE between the two granitoids suggest that they were fractionated by different mineral assemblages. In the gray monzogranites, all REE decrease markedly with decreasing B parameter (B=mol. Ti+Fe+Mg) but the inter-element ratios keep almost constant. This suggests that the modal proportions of REE-fractionating minerals were constant. The pink granite shows a marked increase in LREE/HREE with decreasing B parameter which probably reflects changes in the modal fraction of accessories and other possible major minerals. Another difference dwells in the Eu anomaly, nearly constant in the pink-red granite but decreasing with the B parameter in the gray monzogranite.

Major element modeling

Geochemical models were performed and displayed in binary diagrams of A/CNK (Al_2O_3 / CaO +Na_2O +K_2O molar) *vs*. mafic index (M = MgO + FeO_t molar). Different models were tested to investigate the geochemical variation of these granitoids (Fig. 9). Fractional crystallization processes were tested using crystallization/mass balance equations with plagioclase (Pl), biotite (Bt) and amphibole (Amp). Analytical data for these minerals were taken from Table I. Titanite (Ttn) was not included due to its low modal proportions and its appearance mainly during the late stages of crystallization. K-feldspar (Kfs) was also not considered because its fractionation leads to Ca increase and K decrease, trends opposed to the observed data. Amphibole modal abundance is very low (<1.5-0.5%) and fractionation amounts higher than 1-0.5% are not realistic. This indicates that amphibole has not played any important role in crystal fractionation processes at least in the studied compositional range. The results shown in Figure 9A indicate that a combination of Bt ± Pl fractionation could account for part of the gray monzogranite geochemical variability. On the other hand the trends of K, Na, P and A/CNK cannot be reproduced with such a model. Also Bt + Pl fractionation cannot link the gray and the pink-red granites effectively, especially for K, Na, P and A/CNK. The scatter shown by the samples of the pink-red granite and the differences in REE between both granites discredit a fractional crystallization process.

A magma mixing test was done using the compositions of a pink-red leucogranite and the granodiorite/quartz-monzodiorite enclave. Such a mixing model could explain the composition of the gray monzogranite samples as observed in Figure 9B. Although it seems to work well, it cannot explain the Na_2O, Al_2O_3, Zr and REE contents of the gray monzogranite and therefore cannot be considered as a feasible process. Furthermore, nearly 20-60% of granodiorite/quartz-monzodiorite component would have been necessary to generate the observed compositional range, whereas the observed volume of these enclaves is much lower.

The geochemical diversity of these granites could have been inherited from the source and melting process. Peritectic phases formed during melting could have been incorporated into the initial melts in different modal amounts explaining the geochemical diversity of the granites (Stevens *et al.*, 2007; Clemens and Stevens, 2012). We have modeled the entrainment of different peritectic phases that result from dehydration melting reactions (orthopyroxene: Opx, clinopyroxene: Cpx, garnet: Grt, ilmenite: Ilm, and plagioclase: Pl) and from water fluxed partial melting (amphibole: Amp). The initial melt chosen was the less mafic sample of the gray monzogranite and was mixed with different amounts of possible peritectic phases. Crustal melting involving peritectic phases such as garnet or cordierite, typical in melting of metapelites (biotite + aluminosilicate (Als) + quartz (Qz) = garnet/cordierite (Crd) + K-feldspar + melt) would generate a trend of increasing A/CNK and increasing maficity with the increasing amount of garnet or cordierite entrained. This is not the case of the Porriño granites, at least for the gray monzogranite.

Amphibole as a peritectic phase would imply that the melting event occurred in the presence of free H_2O (Reichardt and Weinberg, 2012; Weinberg and Hasalová, 2015) what is rather uncommon. Such a model matches the observed A/CNK variations with maficity but not for other elements. In combination with other possible peritectic phases such as orthopyroxene, clinopyroxene, plagioclase and garnet, it would be able to explain most of the observed major element variations of the studied rocks. Wet melting of different suites of rocks (metagranitoids and orthogneisses of variable compositions) can generate plagioclase and orthopyroxene as peritectic phases (Weinberg and Hasalová, 2015) but it is not a frequent case and without such phases our model would not be able to match some element variations, especially Al_2O_3 and CaO. Amphibole as a peritectic phase could also be produced by dehydration melting of metabasalts by a reaction producing peritectic Amp + Cpx + Opx + Grt, but without plagioclase as a reaction product. Clinopyroxene and orthopyroxene as peritectic phases would occur in dehydration melting

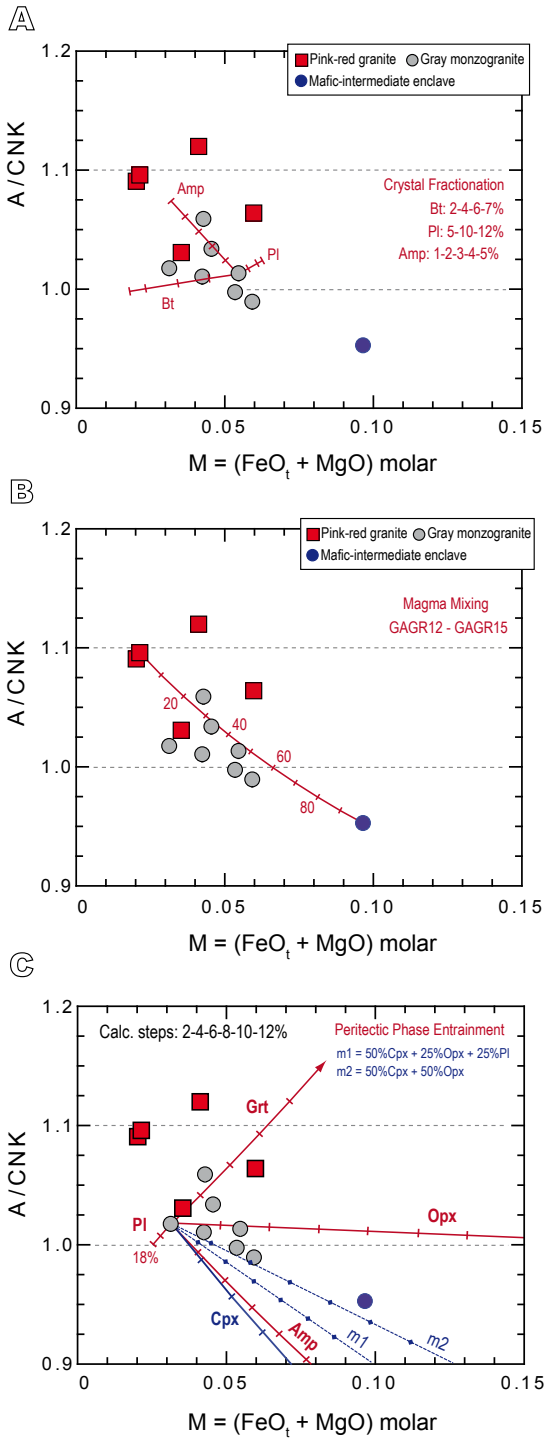

FIGURE 9. Geochemical models using major elements. Peraluminous index (A/CNK) and Maficity (FeO_t + MgO, in molar proportions) are used to display the results. A) Fractional crystallization using linear mixing equations (Ragland, 1989). B) Magma mixing with the pink-red granite and tonalite as end members. C) Peritectic phase entrainment taking the most leucocratic gray monzogranite as the initial melt composition. Different combinations of a peritectic assemblage formed by Cpx + Opx ± Pl (among other minor phases: ilmenite, apatite, garnet) are possible to explain the data. Amphibole, biotite and plagioclase are from Table I. Garnet and orthopyroxene are from the Nijar dacite (Acosta-Vigil, 2012), clinopyroxene is from the Caldas de Reis pluton (Cuesta, 1991).

processes of metagreywackes and intermediate/mafic igneous derived lithologies (Bt + Pl + Qz = Opx ± Cpx ± Grt + melt; Amp + Qz = Opx + Cpx ± Grt + melt). If we consider these as the only peritectic phases (Cpx/Opx) the calculated geochemical trends are close to the observed ones. If we consider plagioclase as a peritectic phase together with Cpx + Opx, then different combinations of Cpx + Opx + Pl could account for the observed trends in most of the major elements (Fig. 9C). A reasonable match for the observed trends is obtained by a Opx/Cpx ratio of ≈ 50:50 with little or no plagioclase. Nevertheless, some peritectic plagioclase is needed to account for the Al_2O_3-CaO variations. The maximum amount of entrained assemblage (Cpx + Opx + Pl and/or Cpx + Opx) necessary to explain the geochemical data is 10 - 12% (Fig. 9C). In order to match for the observed Ti and P contents, small amounts of ilmenite and restitic apatite (≈ 0.1-0.5%) would also be needed in the entrained assemblage that would then consist of Cpx + Opx ± Pl ± Ilm ± apatite (Ap). Both clinopyroxene and orthopyroxene can form part of the entrained assemblage, yet clinopyroxene leads to lower A/CNK and would point to melting of an intermediate-mafic igneous protolith. Furthermore, clinopyroxene contains much higher REE than orthopyroxene and similar patterns as amphiboles (Bea, 1996; Smith, 2014) and therefore its entrainment could account for part of the REE observed variability. Garnet could also form part of this theoretical peritectic assemblage as long as its modal abundance remained low (< 2%). This kind of dehydration melting reaction (Bt + Amp + Qz + Pl^1 = Melt + Pl^2 +Cpx + Opx + Ilm ± Grt) is described in Clemens *et al.* (2011) and Clemens and Stevens (2012) and is considered an important melting reaction to produce I-type granitoids.

REE-modeling

The contrasting behavior of REE of the two main granitoid units is well displayed by the ratios of Dy/Dy* *vs.* Dy/Yb (Davidson *et al.*, 2014), where $Dy^* = La^N / (La^{N4/13} * Yb^{(n)9/13})$. This is a measure of the REE concavity (Dy/Dy*) and gradient (Dy/Yb) that can be easily displayed and linked to specific petrogenetic processes in a binary diagram (Fig. 10A; B). To study the effect of fractionation and/or entrainment of minerals on the bulk-rock REE patterns, we have modeled the effects of amphibole (Table II), zircon, allanite and titanite (Gregory *et al.*, 2009). These phases are the main REE carriers in our study rocks. The results indicate that an exclusive crystal fractionation of zircon (Zrn) or allanite (Aln) cannot explain the observed bulk-rock REE patterns. Titanite is mainly a late crystallizing phase and its fractionation was probably very restricted. Amphibole fractionation (or clinopyroxene, which has a similar REE amount and pattern) shows a better fit to the data, but about 8% of amphibole fractionation would be necessary, whereas there is only 0.5-1.5% of amphibole

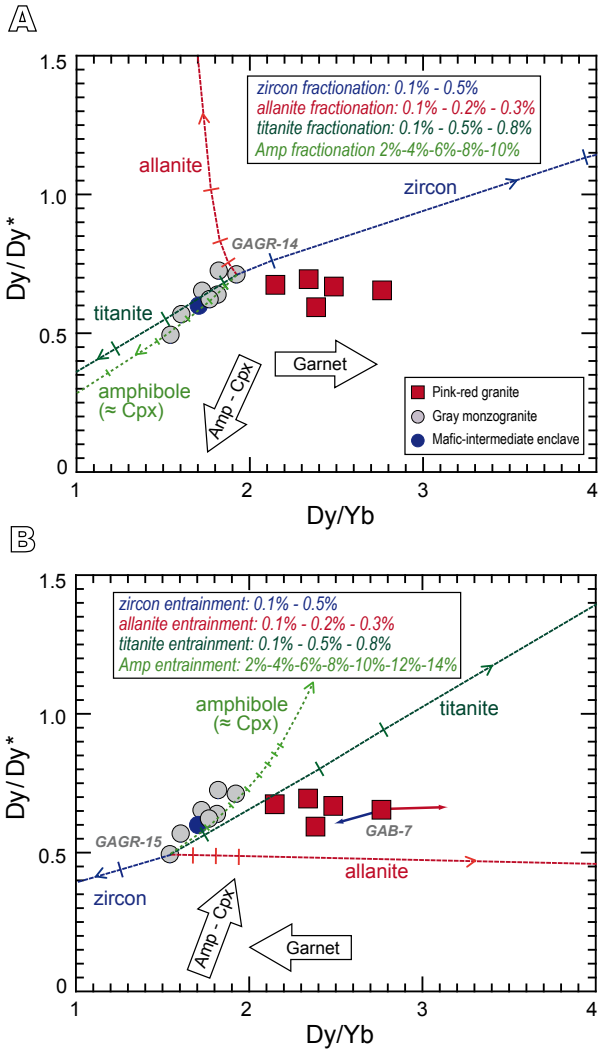

FIGURE 10. Dy/Dy* *vs.* Dy/Yb diagram for representing REE pattern as a single point (Davidson *et al.*, 2014). Crystal fractionation (A) and crystal entrainment or accumulation processes (B) were modeled using standard mass balance equations (Ragland, 1989). The mineral phases used in the modeling are: amphibole from Table I; zircon and titanite from Pe1 granodioritic orthogneis (Gregory *et al.*, 2009); and allanite from Pe11 granodioritic migmatite (Gregory *et al.*, 2009). Arrows of amphibole/clinopyroxene and garnet are from Davidson *et al.* (2014). GAGR-14: starting composition for the fractionation models. GAGR-15 and GAB-7: starting compositions for the entrainment models.

in these rocks. Crystal entrainment models (Fig. 10B) do not have these restrictions and indicate that the best fit to the data would be an entrainment of amphibole (or/and clinopyroxene) ± zircon ± titanite for the gray monzogranite. In the case of the pink granite, entrainment of garnet ± zircon is the best possible match.

Isotope geology and source rocks

The calculated $^{87}Sr/^{86}Sr_{295Ma}$ varies from 0.70186 to 0.71022 in the pink-red granite but it is more constant,

between 0.70516 and 0.70659, in the gray monzogranite and the mafic-intermediate enclave (Table V, ELECTRONIC APPENDIX I; Fig. 11). The εNd_{295Ma} values of the three granitoids are similar (pink-red granite: -0.86, -1.55; gray monzogranite: -0.53, -0.57; mafic intermediate enclave: -1.28) and higher than that of S-type granite rocks and metasedimentary protoliths of the Variscan massif (Bea *et al.*, 2003). These Sr-Nd isotope data indicate a similarity of the gray monzogranite-enclaves with some mafic granulites typical of the lower continental crust (Pérez-Soba and Villaseca, 2010). The pink-red granite shows very variable $^{87}Sr/^{86}Sr_{295Ma}$ having some values similar to intermediate-felsic granulites and other closer to mafic rocks (Fig. 11). Its εNd_{295Ma} is high and can indicate a mafic and juvenile crustal source. These contrasting features suggest that the pink-red granite is made by mixing and/or contamination of rocks/melts of contrasting compositions, or generated by disequilibrium melting processes (McLeod *et al.*, 2012).

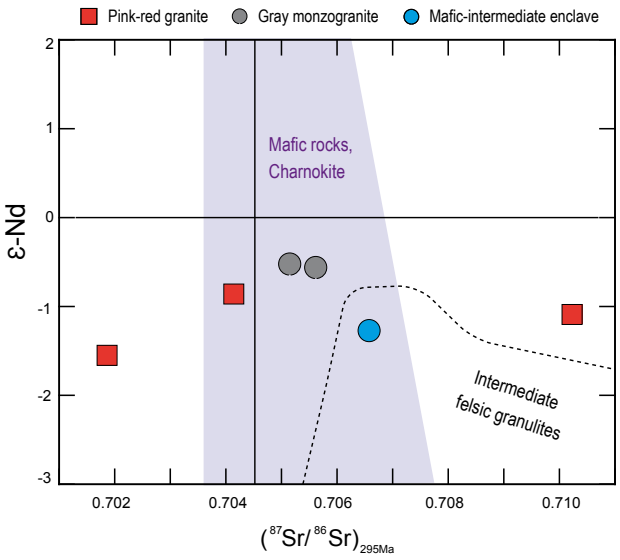

FIGURE 11. Initial Sr isotope ratio calculated at t = 290Ma and epsilon Nd values (ε-Nd) for the the Porriño Pluton (red-pink granites and grey monzogranite + enclave). Field boundaries are from Pérez-Soba and Villaseca (2010). The considerable spread of Sr isotope initial values of the pink-red granite contrasts with the more restricted values of the enclave and gray monzogranite.

Model for the evolution of the Porriño post-tectonic granitoid

i) Based on the data presented, we propose that the pink-red granite is not derived from magmatic differentiation of the gray monzogranite. Its composition, close to some A-type granites, Ca-poor peraluminous, with high Fe/Fe+Mg, $Sr_i \leq 0.710$ and leucocratic nature could derive from low to very low melt fractions from the restitic gray monzogranite protolith, and/or from other, dehydrated-restitic, metasedimentary rocks.

ii) The gray monzogranite derives from melting of metaigneous mafic - intermediate plutonic/volcanic rocks ± metagreywackes in the lower crust. Entrainment of peritectic Cpx + Opx ± Pl ± Ilm and accessories such as ± Zrn ± Ttn ± Ap (restitic) occurred during the melting process. During melt segregation and ascent, Cpx/Opx reacts to form Amp + Bt, as observed in other similar granitoids (Cuesta, 1991) and also in a considerable variety of intermediate magmas (Smith, 2014). The peritectic plagioclase entrained in the melt batches would explain the Ca-rich nature of the magma that would later enhance Ttn + Aln crystallization. Additional phases such as quartz, K-feldspar, more sodic plagioclase and biotite crystallized from the melt during ascent and emplacement at P≈2.5-3.5kbar. This evolution could explain the generation of some post-tectonic I-type granitoids in the northwestern branch of the Iberian Variscan belt.

iii) The melting process was probably conditioned by the previous extract of a high volume of S-type, syn-tectonic magmas. The melting to generate the post-tectonic granitoids was due to progressive heat input where the first lower crustal lithologies to melt were those that still had water bearing minerals (biotite and amphibole). The initial heat input was used in the melting process that generated the gray I-type monzogranites. A mafic-intermediate source rock is favored by the Sr-Nd isotopes and the geochemical modeling. As the heat flow raised, low melt fractions from previous restitic sources were also produced and generated the pink-red granite showing intermediate features between A- and I-types. Disequilibrium melting (or mixed sources) would account for the observed isotopic variability, especially in the $^{87}Sr/^{86}Sr_{295Ma}$ values. Further heat input would have generated higher melt fractions giving rise to more typical A-type granites and/or peralkaline granites, characterized by very high HFSE and REE contents. Nevertheless, in our study region such stages were not reached probably due to a decrease in the heat flux in the waning of the orogenic processes. A similar hypothesis in both the melting process and sources has been proposed by Miao *et al.* (2015) to explain the association of Triassic calc-alkaline and alkaline granitoids in Qiman Tagh, East Kulun, China.

Comparison with similar granites and generalization of the model

The petrogenesis proposed for the Porriño granites could be in part valid for other I-type granitoids of the NW Iberian Variscan massif. One of the most representative of these granitoids is the Caldas de Reis pluton, formed by several granitoid units of different composition (Cuesta, 1991). The most abundant facies within this batholith are similar to those studied here: outer pink-red granites and leucogranites and inner gray monzogranites. The Caldas

de Reis pluton also contains enclaves of tonalites in which amphibole includes relict clinopyroxene. Porriño, Caldas de Reis and other post-tectonic Variscan granitoids show typical I-type features with some facies having characteristics of A-type granites and a similar mineralogy. The common presence of amphibole, locally including clinopyroxene, is in accordance with a perictectic entrainment process such as the one proposed here. This would help to explain the compositional diversity of these granitoids in a more satisfactory way than the fractional or equilibrium crystallization classic schemes.

The reason for the late production of I-type granitoids with some A-type affinities could be related to the widespread previous extract of S-type syn-tectonic granites from the lower/middle crust (Fig. 12C). The most important S-type magmatic event could be due to continental collision and accumulation of radiogenic heat after the Variscan crustal thickening (Bea, 2012). The initiation of lithospheric delamination could have also been another heat source at this stage. The resultant residual lower to middle crust was probably dehydrated and partly restitic after such melt extraction (Fig. 12C). Given the nature of the melts produced, strongly peraluminous two mica ± Als ± Grt granites, the dehydration melting processes probably involved muscovite (Ms) ± biotite of fertile metapelite protoliths (Ms + Pl + Qz = Als +Kfs + Melt; Spear 1993. Bt + Als + Qz = Grt/Crd + Kfs + Melt; Le Breton and Thompson, 1988; Spear, 1993). Other lithologies such as meta-greywackes (orthogneisses) and intermediate-mafic plutonic/meta-volcanic rocks probably did not melt or melting was minor. The lower to middle crust hence became partly restitic. Orogenic collapse, extensional processes (lowering of pressure) and/or the peak of delamination of previously thickened lithosphere (lithospheric mantle replacement by asthenosphere, Gutiérrez-Alonso *et al.*, 2011) finally lead to the last magmatic events accounting for the I-type granitoids with minor units showing A-type features. The protoliths of these magmas could have been the lithologies previously unmelted (or with very low melt extraction) such as intermediate-mafic plutonic and volcanic rocks, meta-greywackes or the residues after the previous S-type magmatic event. Heating during this last magmatic event could have caused different melting stages affecting the same protolith or mixed protoliths (Fig. 12D).

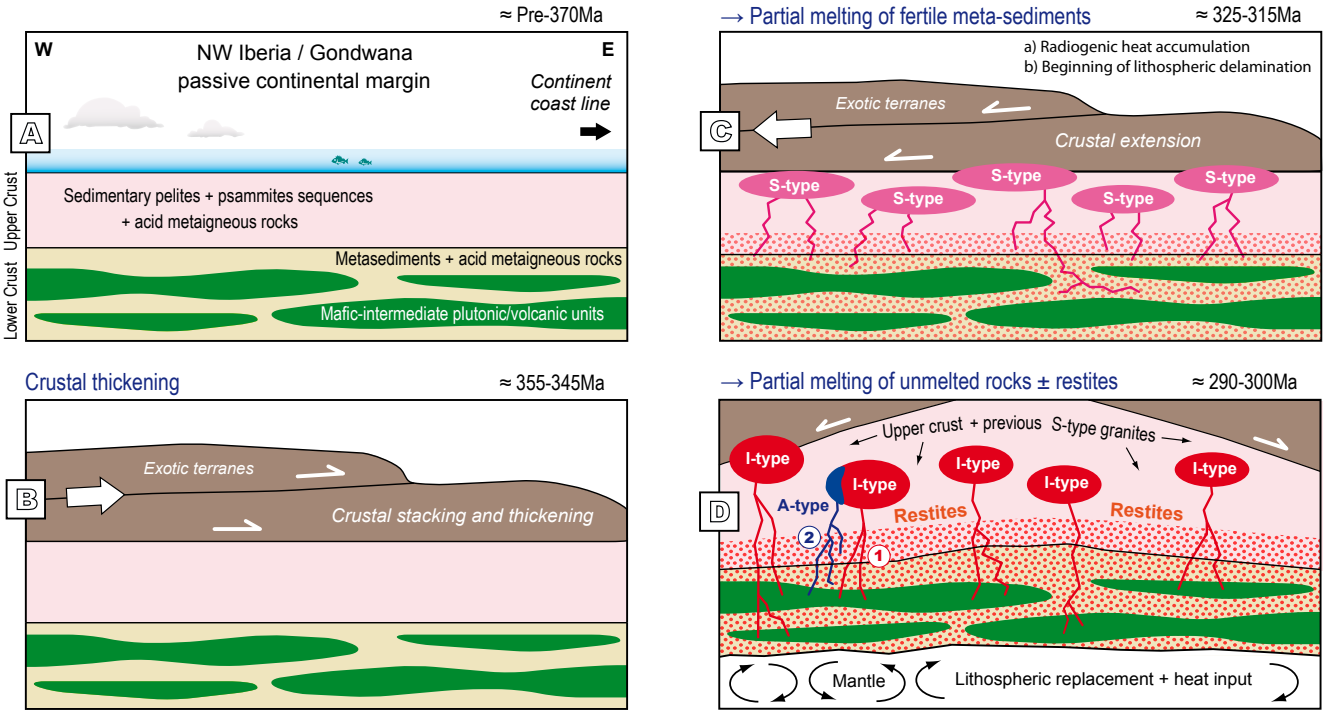

FIGURE 12. Sketch (not to scale) of the magmatic evolution of the NW Iberian massif and the generation of post-tectonic I-type granitoids with minor associated A-types such as the case of the Porriño pluton. A) Approximate pre-variscan continental crust with interlayered mafic-intermediate plutonic and volcanic units in the lower crust. The rest of the main rocks would be fertile lithologies such as siliciclastic sediments and acid volcanic-plutonic rocks. B-C) Variscan collision tectonics produced crustal thickening, radiogenic heat accumulation and onset of lithospheric delamination processes that generated melting of the more fertile rocks (middle and lower crust) and produced mostly S-type granites. This event exhausted the more fertile rocks, leaving restites and unmelted lithologies such as mafic-intermediate plutonic and volcanic rocks. D) Subsequent tectonic extension and lithospheric delamination replacement generated enough heat to the melt mafic-intemediate units of the middle-lower crust and formed I-type granitoids (1). Contemporaneous melting of restites could have generated some magmatism with A-type features (2).

A similar model with depletion of fertile metasedimentary source rocks after S-type granite generation, resulting in production of I- and A-type granites, has been recently presented by Turnbull *et al*. (2016) for the 370Ma granitic magmatism of New Zealand.

The final result of the Variscan orogeny was the production of an important and widespread granitic to granodioritic upper crust and a residual or restitic lower/middle crust from which magmas were extracted. This Variscan lower crust was afterwards partly involved in several alpine orogenic events (Alps, Pyrenees, Betics) were crustal thickening was substantial but without important granitic magmatism. The reasons for this absence or low abundance of alpine granitoid batholiths might lie in the very residual or restitic nature of the Variscan lower/middle crust involved (Vielzeuf and Montel, 1994) that would have needed much higher P-T conditions to melt than those reached during the alpine orogeny.

CONCLUSIONS

The Variscan Porriño post-tectonic pluton is formed by two granitoid units (a pink-red granite and a gray monzogranite) and intermediate-mafic enclaves included within the gray monzogranite.

The pink-red granite shows differences in mineralogy, geochemistry (lower Ca, higher K/Na and Fe/Fe+Mg, etc.) and isotope geology indicating either a specific source or different melting conditions. We propose that its source was formed by restitic rocks (metasedimentary and mafic-intermediate rocks). These protoliths were affected by a low melting percentage, leading to leucocratic melts with mixed features of I- and A-type granites as observed in the pink-red Porriño granite. Disequilibrium melting processes or different sources could explain the variation in the initial Sr isotopic values (0.703-0.710).

The gray monzogranite and its mafic-intermediate enclaves share a similar source and petrogenesis. The source rocks could have been mafic-intermediate volcanic or plutonic rocks located in the middle to lower continental crust. Partial melting of this protolith under water undersaturated conditions likely generated a granitic melt and perictectic phases such as Cpx + Opx ± Pl ± Ilm (coexisiting with restitic accessories like ± Zrn ± Ttn ± Ap). Different amounts of mixing between this peritectic assemblage and the granitic liquid can account for the observed geochemical variation.

Previous orogenic melting events, related to Variscan crustal thickening, produced mainly S-type magmatism leaving middle to lower crustal meta-sedimentary restites ± meta-greywackes (orthogneisses) and mafic-intermediate rocks that either did not melt or in which melt extraction was very reduced. When orogenic collapse was at its peak, a combination of pressure decrease and lithospheric replacement by hot asthenosphere probably led to new melting of the lower crustal meta-greywakces/mafic-intermediate rocks generating the I-type postectonic magmatism. Associated A-types could have developed if the melting affected restitic rocks from early melting events.

ACKNOWLEDGMENTS

This research has been partially financed by the Spanish grant CGL2013-40785-P. We thank the editors, G. Gutiérrez-Alonso and two anonymous reviewers for the comments and corrections which helped to improve the present manuscript. This is the IBERSIMS publication Nº46.

REFERENCES

Abdel-Rahman, A.M., 1994. Nature of biotites from alkaline, calc-alkaline and peraluminous magmas. Journal of Petrology, 35, 525-541.

Altherr, R., Holl, A., Hegner, E., Langer, C., Kreuzer, H., 2000. High-potassium, calc-alkaline I-type plutonism in the European Variscides: northern Vosges (France) and northern Schwarzwald (Germany). Lithos, 50, 51-73.

Anderson, J.L., 1983. Proterozoic anorogenic granite plutonism of North America. Geological Society of America Memoir, 161, 133-154.

Anderson, J.L., Smith, D.R., 1995. The effects of temperature and fO_2 on the Al-in-hornblende barometer. American Mineralogist, 80, 549-559.

Aranguren, A., Román-Berdiel, T., Cuevas, J., Tubía, J.M., 2000. Fábrica magnética del plutón de La Tojiza (Galicia). Revista de la Sociedad Geológica de España, 13(1), 121-130.

Barrera Morate, J.L., Farias Arquer, P., González Lodeiro, F., Marquínez García, J., Martín Parra, L.M., Martínez Catalán, J.R., Olmo Sanz, A., Pablo Maciá, J.G. de, 1989. Hoja y Memoria del Mapa Geológico de España E 1:200.000 nº 17 (Orense-Verín). Instituto Geológico y Minero de España (IGME), Primera edición, 284pp.

Bea, F., 1996. Residence of REE, Y, Th and U in granites and crustal protoliths; implications for the chemistry of crustal melts. Journal of Petrology, 37(3), 521-522.

Bea, F., 2004. La naturaleza del magmatismo de la Zona Centroibérica: Consideraciones generales y ensayo de correlación. In: Vera, J.A. (ed.). Sociedad Geológica de España–Instituto Geológico y Minero de España (SGE-IGME),. Madrid, 128-133.

Bea, F., 2012. The sources of energy for crustal melting and the geochemistry of heat-producing elements. Lithos, 153, 278-291.

Bea, F., Pereira, M.D., Corretgé, L.G., Fershtater, G.B., 1994. Differentiation of strongly peraluminous, perphosphorous granites: The Pedrobernardo pluton, central Spain. Geochimica et Cosmochimica Acta, 58(12), 2609-2627.

Bea, F., Montero, P., Stroh, A., Bassner, J., 1996. Microanalysis of minerals by an excimer UV-LA-ICP-MS system. Chemical Geology, 133, 145-156.

Bea, F., Montero, P., Zinger, T., 2003. The nature and origin of the granite source layer of central Iberia: evidence from trace element, Sr, and Nd isotopes, and zircon age patterns. Journal of Geology, 11, 579-595.

Bea, F., Fershtater, G.B., Montero, P., Smirnov, V.N., Molina, J.F., 2005. Deformation-driven differentiation of granitic magma: the Stepninsk pluton of the Uralides, Russia. Lithos, 81, 209-233.

Bellido Mulas, F., González Lodeiro, F., Klein, E., Martínez Catalán, J.R., Pablo Maciá, J.G. de, 1987. Las rocas graníticas hercínicas del norte de Galicia y occidente de Asturias. Colección Memorias Instituto Geológico y Minero de España, 101, 157pp.

Bellido, F., Monteserín, V., Gumiel, P., Ferrero, A., Baltuille, J.M., López, M.T., 2005. Características petrológicas y geoquímicas de las principales variedades de granitos ornamentales del macizo de "O Porriño" (SO de Galicia). Boletín Geológico y Minero, 116(4), 331-349.

Black, L.P., Kamo, S.L., Allen, C.M., Aleinikoff, J.A., Davis, D.W., Korsch, J.R., Foudolis, C., 2003. TEMORA 1: a new zircon standard for Phanerozoic U-Pb geochronology. Chemical Geology, 200, 155-170.

Bonin, B., 2004. Do coeval mafic and felsic magmas in post-collisional to within-plate regimes necessarily imply two contrasting, mantle and crustal, sources? A review. Lithos, 78, 1-24.

Bruiyn, H., Westhuizen, W.A., van der, Schoch, A.E., 1983. The estimation of FeO, F and H_2O^+ by regression in microprobe analyses of natural biotite. Trace and Microprobe Techniques, 114, 399-412.

Capdevila, R., Floor, P., 1970. Les differents types de granites hercyniens et leur distribution dans le Nord-Ouest de l'Espagne. Boletín Geológico y Minero, 81, 215-225.

Capdevila, R., Corretgé, L.G., Floor, P., 1973. Les granitoides varisques de la Meseta Ibérique. Bulletin de la Société Géologique de France, 15, 209-228.

Castro, A., 2013. The off-crust origin of granite batholiths. Geoscience Frontiers, 5, 63-75.

Castro, A., Patiño-Douce, A.E., Corretgé, L.G., de la Rosa, J.D., El-Biad, M., El-Hmidi, H., 1999. Origin of peraluminous granites and granodiorites, Iberian massif, Spain: an experimental test of granite petrogenesis. Contributions to Mineralogy and Petrology, 135, 255-276.

Chappell, B.W., White, A.J.R., 1992. I- and S-type granites in the Lachlan Fold Belt. Transactions of the Royal Society of Edinburgh: Earth Sciences, 83, 1-26.

Clemens, J.D., Bezuidenhout, A., 2014. Origins of co-existing diverse magmas in a felsic pluton: the Lysterfield Granodiorite, Australia. Contributions to Mineralogy and Petrology, 167, 991. DOI: 10.1007/s00410-014-0991-9.

Clemens, J.D., Stevens, G., 2012. What controls chemical variation in granitic magmas? Lithos, 134-135, 317-329.

Clemens, J.D., Stevens, G., Farina, F., 2011. The enigmatic sources of I-type granites: the perictectic connection. Lithos, 126, 174-181.

Corretgé, L.G., Suárez, O., Llana, R., 1981. Variaciones petrográficas y geoquímicas en plutones graníticos: zonación y criptozonación en batolitos epizonales. Cuadernos del Laboratorio Xeoloxico de Laxe, 2, 11-31.

Corretgé, L.G., Suárez, O., Galán, G., Fernández-Suárez, J., 2004. Zona Asturoccidental-leonesa: Magmatismo. In: Vera, J.A. (ed.). Geología de España. Sociedad Geológica de España – Instituto Geológico y Minero de España (SGE-IGME), Madrid, 63-68.

Cottard, F., 1979. Pétrologie structurale et métallogénie du complexe granitique de Lovios-Geres. Le modèle de mise en place de la mine de Las Sombras (Sn-W-Mo-Bi) (Sud Galice-Espagne). Thèse 3éme cycle. Université Nancy I, 226pp.

Cuesta, A., 1991. Petrología granítica del plutón de Caldas de Reis (Pontevedra, España). Estructura, mineralogía, geoquímica y petrogénesis. Laboratorio Xeoloxico de Laxe, Serie Nova Terra, 5, 363pp.

Cuesta, A., Gallastegui, G., 2004. Magmatismo de la Zona Centroibérica: Galicia occidental. In: Vera, J.A. (ed.). Geología de España. Sociedad Geológica de España – Instituto Geológico y Minero de España (SGE-IGME), Madrid, 96-100.

Czamanske, G.K., Ishihara, S., Atkin, S.A., 1981. Chemistry of rock-forming minerals of the Cretaceous - Paleocene batholith in southwestern Japan and implications for magma genesis. Journal of Geophysical Research, 86(B11), 10431-10469.

Dall'Agnol, R., Teixeira, N.P., Rämö, O.T., Moura, C.A.V., Macambira, M.J.B., Oliveira, D.C., 2005. Petrogenesis of the Paleoproterozoic, rapakivi, A-type granites of the Archean Carajás Metallogenic Province, Brazil. Lithos, 80, 101-129.

Dall'Agnol, R., Oliveira, D.C., 2007. Oxidized, magnetite-series, rapakivi-type granites of Carajás, Brazil: implications for classification and petrogenesis of A-type granites. Lithos, 93, 215-233.

Dallmeyer, R.D., Martínez Catalán J.R., Arenas, R., Gil Ibarguchi, J.I., Gutiérrez Alonso, G., Farias, P., Aller, J., Bastida, F., 1997. Diachronous Variscan tectonothermal activity in the NW Iberian Massif: Evidence from $^{40}Ar/^{39}Ar$ dating of regional fabrics. Tectonophysics, 277, 307-337.

Davidson, J., Turner, S., Plank, T., 2013. Dy/Dy*: Variations arising from mantle sources and petrogenetic processes. Journal of Petrology, 54(3), 525-537.

Debon, F., Lemmet, M., 1999. Evolution of Mg/Fe ratios in late variscan plutonic rocks from the external crystalline massifs of the Alps (France, Italy, Switzerland). Journal of Petrology, 40(7), 1151-1185.

Eby, N., 2011. A-type granites: magma sources and their contribution to the growth of the continental crust. Seventh Hutton Symposium on Granites and Related Rocks, pp. 50-51.

Elliot, B.A., 2003. Petrogenesis of post-kinematic magmatism of the Central Finland Granitoid Complex II; sources and magmatic evolution. Journal of Petrology, 44(9), 1681-1701.

England, P.C., Thompson, A.B., 1986. Some thermal and tectonic models for crustal melting in continental collision belts. In: Coward, M.P., Ries, A.C., (eds.). Collision Tectonics. Geological Society of London Special Publication, 19, 83-94.

Fernández-Suárez, J., Dunning, G.R., Jenner, G.A., Gutiérrez-Alonso, G., 2000. Variscan collisional magmatism and deformation in NW Iberia: constraints from U-Pb geochronology of granitoids. Journal of the Geological Society (London), 157, 565-576.

Finger, F., Steyer, H.P., 1990. I-type granitoids as indicators of late Paleozoic convergent ocean-continent margin along the southern flank of the central European Variscan orogeny. Geology, 18, 1207-1210.

García Garzón, J., 1987. Datación por el método Rb-Sr de dos muestras de granito de Galicia: granito tipo Padrón y granito tipo Porriño. Boletín Geológico y Minero, 98, 107-110.

González-Menéndez, L., 1998. Petrología y geoquímica del batolito de Nisa-Alburquerque (Alto Alentejo, Portugal, Extremadura, España). PhD Thesis, University of Granada, Spain, 223pp.

Govindaraju, K., Potts, P.J., Webb, P.C., Watson, J.S., 1994. Report on Whin Sill Dolerite WS-E from England and Pitscurrie Micrograbbro PM-S from Scotland: assessment by one hundred and four international laboratories. Geostandards Newsletters, 18, 211-300.

Gregory, C.J., Buick, I.A., Hermann, J., Rubatto, D., 2009. Mineral-scale Trace Element and U-Th-Pb Age Constraints on Metamorphism and Melting during the Petermann Orogeny (Central Australia). Journal of Petrology, 50(2), 251-287.

Gutiérrez-Alonso, G., Fernández-Suárez, J., Weil, A.B., 2004. Orocline triggered lithospheric delamination. In: Weil, A.B., Sussman, A. (eds.). Paleomagnetic and structural analysis of orogenic curvature. Geological Society of America, Special Paper, 383, 121-131.

Gutiérrez-Alonso, G., Fernández-Suárez, J., Jeffries, T.E., Johnston, S.T., Pastor-Galán, D., Brendan Murphy, J., Franco, M.P., Gonzalo, J.C., 2011. Diachronous post-orogenic magmatism within a developing orocline in Iberia, European Variscides. Tectonics, 30(5), TC5008.

Hirata, T., Nesbitt, R.W., 1995. U–Pb isotope geochronology of zircon: evaluation of the laser probe-inductively coupled plasma mass spectrometry technique. Geochimica et Cosmochimica Acta, 59, 2491-2500.

Kemp, A.S.I., Hawksworth, C.J., Foster, G.L., Paterson, B.A., Woodhead, J.D., Hergt, J.M., Gray, C.M., Whitehouse, M.J., 2007. Magmatic and crustal differentiation history of granitic rocks from Hf-O isotopes in zircon. Science, 315, 980-983.

King, P.L., White, A.R.J., Chappel, B.W., Allen, C.M., 1997. Characterization and origin of aluminous A-type granites from the Lachlan Fold Belt, Southeastern Australia. Journal of Petrology, 38(3), 371-391.

Le Breton, N., Thompson, A.B., 1988. Fluid absent (dehydration) melting of biotite in metapelites in the early stages of anatexis. Contributions to Mineralogy and Petrology, 99, 226-237.

Leake, B.E., Woolley, A.R., Arps, C.E.S., Birch, W.D., Gilbert, M.C., Grice, J.D., Hawthorne, F.C., Kato, A., Kisch, H.J., Krivovichev, V.G., Linthout, K., Laird, J., Mandarino, J., Maresch, W.V., Nickel, E.H., Rock, N.M.S., Schumacher, J.C., Smith, D.C., Stephenson, N.C.N., Ungaretti, L., Whittaker, E.J.W., Youzhi, G., 1997. Nomenclature of amphiboles: report of the subcommittee on amphiboles of the International Mineralogical Association Commission on New Minerals and Mineral Names. Mineralogical Magazine, 61, 295-321.

McLeod, C.L., Davidson, J.P., Nowell, G.M., Shanaka, L.S., 2012. Disequilibrium melting during crustal anatexis and implications for modeling open magmatic systems. Geology, 40, 435-438.

Mendes, A.C., Dias, G., 2004. Mantle-like Sr–Nd isotope composition of Fe-K subalkaline granites: the Peneda-Gerês Variscan massif (NW Iberian Peninsula). Terra Nova, 16, 109-115.

Merino Martínez, E., Villaseca, C., Orejana, D., Pérez-Soba, C., Belousova, E., Andersen, T., 2014. Tracing magma sources of three different S-type peraluminous granitoid series by in situ U-Pb geochronology and Hf isotope zircon composition: The Variscan Montes de Toledo batholith (central Spain). Lithos, 200-201, 273-298.

Miao, Y., Feng, C., Zhao, Y., Daxin, L., 2015. Genesis of post-collisional calc-alkaline and alkaline granitoids in QimanTagh, East Kunlun, China. Lithos, 239, 45-59.

Montero, P., Bea, F., 1998. Accurate determination of $^{87}Rb/^{86}Sr$ and $^{147}Sm/^{144}Nd$ ratios by inductively-coupled-plasma mass spectrometry in isotope geoscience: an alternative to isotope dilution analysis. Analytica Chimica Acta, 358, 227-33.

Nakamura, N., 1974. Determination of REE, Ba, Fe, Mg, Na and K in carbonaceous and ordinary chondrites. Geochimica et Cosmochimica Acta, 38(5), 757-775.

Pérez-Estaún, A., Bea, F., 2004. Macizo Ibérico. In: Vera J.A. (ed.). Geología de España. Sociedad Geológica de España–Instituto Geológico y Minero de España (SGE-IGME), Madrid, 19-230.

Pérez-Soba, C., Villaseca, C., 2010. Petrogenesis of highly fraccionated I-type peraluminous granites: La Pedriza pluton (Spanish Central System). Geologica Acta, 8(2), 131-149.

Ragland, P.C., 1989. Basic Analytical Petrology. Oxford University Press, 369pp.

Reichardt, H., Weinberg, R.F., 2012. Hornblende chemistry in meta- and diatexites and its retention in the source of leucogranites: an example from the Karakoran shear zone, NW India. Journal of Petrology, 53, 1287-1318.

Ries, A.C., 1979. Variscan metamorphism and K-Ar dates in the Variscan Fold Belt of S Brittany and NW Spain. Journal of the Geological Society (London), 136, 89-103.

Roberts, M.P., Clemens, J.D., 1993. Origin of high-potassium, calc-alkaline, I-type granitoids. Geology, 21, 825-828.

Rubio Pascual, F.J., Arenas, R., Martínez Catalán, J.R., Rodríguez Fernández, L.R., Wijbrans, J.R., 2013. Thickening and exhumation of the Variscan roots in the Iberian Central System: Tectonothermal processes and $^{40}Ar/^{39}Ar$ ages. Tectonophysics, 587, 207-221.

Simões, P.P., Sant'Ovaia, H., Martins, H.C.B., Dias, G., 2013. The Fe-K subalkaline Monçao-Porriño pluton (NW Portugal): genesis, fabric and SHRIMP U-Pb zircon geochronology. IX Congreso Ibérico - XI Congreso Nacional de Geoquímica, Soria (Spain), 22-23.

Smith, D.J., 2014. Clinopyroxene precursors to amphibole sponge in arc crust. Nature Communications, 5, 4329.

Spear, F.S., 1993. Metamorphic Phase Equilibria and Pressure-Temperature-Time Paths. Mineralogical Society of America, Washington D.C., 799pp.

Statacorp, 2005. Stata Statistical Software, Release 9. College Station, TX, StataCorp LP.

Stevens, G., Villaros, A., Moyen, J.F., 2007. Selective peritectic garnet entrainment as the origin of geochemical diversity in S-type granites. Geology, 35(1), 9-12.

Sylvester, P., 1998. Post-collisional strongly peraluminous granites. Lithos, 45, 29-44.

Thompson, A.B., Connolly, J.A.D., 1995. Melting of the continental crust: Some thermal and petrological constraints on anatexis in continental collision zones and other tectonic settings. Journal of Geophysical Research, 100, 15565-15579.

Turnbull, R., Tulloch, A., Ramenazi, J., Jongens, R., 2016. Extension-facilitated pulsed S-I-A-type "flare-up" magmatism at 370Ma along southeast Gondwana margin in New Zeland: Insights from U-Pb geochronology and geochemistry. Geological Society of America Bulletin, 128(9/10), 1500-1520.

Turner, S., Sandiford, M., Foden, J., 1992. Some geodynamic and compositional constraints on "postorogenic" magmatism. Geology, 20, 931-934.

Vielzeuf, D., Montel, J.M., 1994. Experimental constraints on partial melting in the crust. Mineralogical Magazine, 58A, 940-941.

Villaseca, C., Bellido, F., Pérez-Soba, C., Billström, K., 2009. Multiple crustal sources for post-tectonic I-type granites in the Hercynian Iberian belt. Mineralogy and Petrology, 96, 197-211.

Weinberg, R.F., Hasalová, P., 2015. Water-fluxed melting of the continental crust: a review. Lithos, 212-215, 158-188.

Whalen, J.B., Curry, K.L., Chappell, B.W., 1987. A-type granite: geochemical characteristics, discrimination and petrogenesis. Contributions to Mineralogy and Petrology, 95, 407-419.

Wones, D.R., Eugster, H.P., 1965. Stability of biotite: experiment, theory, and application. American Mineralogist, 50, 1228-1272.

Yenes, M., Álvarez, F., Gutiérrez-Alonso, G., 1999. Granite emplacement in orogenic compressional conditions: the La Alberca-Bejar granitic area (Spanish Central System, Variscan Iberian Belt). Journal of Structural Geology, 21, 1419-1440.

Manuscript received January 2017;
revision accepted October 2017;
published Online October 2017.

ELECTRONIC APPENDIX I

TABLE I. Selected EMP analyses of minerals in the Porriño plutonic rocks (wt.%)

Rock type	Microgranular enclave				Mafic enclave			Gray monzogranite	
Sample	GAGR-6-1				GAGR-15			GAGR-16	GAGR-14
Phase	Amp-Clot		Amp	Amp (a)	Amp	Amp	Amp	Amp	Amp
Texture	Core	Rim	Incl-Pl	Core	Core	Rim	Core	Rim	Aggregate
SiO_2	46.10	44.98	40.17	41.13	43.71	41.61	41.27	40.73	42.76
TiO_2	0.37	0.73	1.08	1.28	1.48	1.62	1.66	1.60	1.28
Al_2O_3	3.75	6.16	8.37	7.91	7.55	8.89	9.47	9.31	7.12
Cr_2O_3	0.02	0.10	0.05	0.09				0.00	0.04
FeO	21.89	23.19	24.77	25.21	25.71	25.93	25.58	26.04	25.12
MnO	0.68	0.75	0.72	0.66	0.57	0.57	0.58	0.71	0.88
MgO	8.57	7.40	5.53	5.44	5.54	4.97	5.02	4.81	5.89
CaO	11.68	11.54	11.33	11.23	10.99	11.32	11.15	10.96	11.22
Na_2O	0.89	1.08	1.40	1.50	1.43	1.42	1.63	1.79	1.41
K_2O	0.52	0.82	1.23	1.11	0.99	1.20	1.33	1.26	0.92
P_2O_5	0.07	0.05	0.03	0.01				0.02	0.03
F	0.40	0.34	0.32	0.32				0.18	0.21
Cl	0.02	0.01	0.06	0.06	0.09	0.07	0.09	0.11	0.06
Total	94.97	97.15	96.47	95.96	98.08	97.61	97.77	97.53	96.94
Fe/(Fe+Mg)	0.56	0.60	0.66	0.69	0.69	0.72	0.71	0.72	0.67

Rock type	M. enclave		Mafic enclave		Gray monzogranite				Pink-red granite		
Label	GAGR-6-1		GAGR-15		GAGR-14		GAGR-16	GAGR-18	GAGR-17		GAGR-5
Phase	Bt (a)	Bt	Bt	Bt	Bt	Bt	Bt	Bt	Bt	Bt	Bt
SiO_2	35.37	34.08	35.62	34.97	35.67	34.52	33.66	36.31	34.13	32.81	34.64
TiO_2	3.61	3.31	4.16	3.59	2.54	3.96	4.01	3.08	3.21	3.87	3.58
Al_2O_3	13.26	13.49	13.67	13.71	14.34	12.82	13.50	13.54	14.38	13.52	13.54
Cr_2O_3	0.05	0.01			0.00	0.00	0.02	0.04	0.00	0.03	
FeO	24.74	25.91	27.11	28.34	26.18	27.94	28.21	28.27	30.80	31.75	32.52
MnO	0.42	0.37	0.22	0.32	0.44	0.40	0.38	0.46	0.39	0.39	0.46
MgO	7.90	6.69	5.98	5.54	6.30	6.13	5.43	5.82	3.00	2.90	2.82
CaO	0.01	0.04	0.03	0.02	0.01	0.00	0.01	0.02	0.01	0.03	0.00
Na_2O	0.02	0.06	0.04	0.05	0.04	0.05	0.06	0.04	0.05	0.09	0.07
K_2O	9.33	9.22	9.19	9.19	9.63	9.32	9.52	9.27	9.04	8.98	9.19
P_2O_5	0.00	0.00			0.00	0.00	0.00	0.01	0.00	0.00	
F	0.81	0.40			0.18	0.43	0.23		0.32	0.75	
Cl	0.05	0.06	0.06	0.04	0.04	0.05	0.04	0.03	0.07	0.08	0.11
Total	95.56	94.24	96.07	95.78	95.36	95.62	95.06	96.89	95.41	95.08	96.85
Fe/(Fe+Mg)	0.64	0.68	0.72	0.74	0.70	0.72	0.74	0.73	0.85	0.86	0.87

Rock type	Microgranular enclave			Mafic enclave		Gray monzogranite			Pink-red granite	
Sample	GAGR-6-1			GAGR-15		GAGR-18			GAGR-5	
Mineral	Pl	(a)		Pl		Pl			Pl	
Texture	Core	Mottled	Rim	Corroded	Mantle	Core	Middle	Rim	Core	Rim
SiO_2	58.18	51.16	63.15	56.46	63.64	57.75	62.62	65.53	61.36	65.62
TiO_2	0.00	0.03	0.00	0.04	0.02	0.01	0.01	0.01	0.00	0.02
Al_2O_3	25.61	30.23	22.75	26.91	22.84	26.36	23.09	21.76	24.25	21.69
Cr_2O_3	0.01	0.00	0.03			0.00	0.01	0.00		
FeO	0.02	0.10	0.14	0.22	0.07	0.02	0.03	0.17	0.08	0.08
MnO	0.00	0.03	0.00	0.00	0.00	0.03	0.00	0.00	0.00	0.01
MgO	0.00	0.01	0.00	0.01	0.01	0.01	0.00	0.00	0.00	0.00
CaO	7.20	12.63	4.28	9.56	9.56	8.84	5.42	2.91	5.53	2.75
Na_2O	7.80	4.69	9.44	6.27	0.00	6.86	8.78	10.11	8.65	10.20
K_2O	0.11	0.07	0.24	0.16	0.00	0.12	0.19	0.15	0.26	0.22
P_2O_5	0.02	0.06	0.01			0.06	0.03	0.02		
F	0.00	0.00	0.10							
Cl	0.00	0.01	0.00	0.01	0.00	0.01	0.00	0.00	0.00	0.01
Total	98.95	99.02	100.13	99.65	100.62	100.07	100.19	100.67	100.14	100.60
An	34	60	20	45	21	41	25	14	26	13

(a) Amphibole (Amp), biotite (Bt), and plagioclase (Pl), used for geochemical modeling

TABLE II. Selected LA-ICP-MS analyses of minerals in the Porriño plutonic rocks (ppm)

Rock type	Gray monzogranite						Pink-red granite							
Sample	GAGR-15-1				GAGR-7				GAGR-17				GAGR-5	
Phase	Amp	Amp	Bt	Pl	Bt	Pl	Kfs	Kfs	Bt	Bt	Pl	Pl	Kfs	Kfs
LI	22.24	16.27	674.37	0.94	1402.70	1.03	3.04	6.60	806.09	1050.74	4.49	4.13	4.02	3.13
Be	15.18	11.39	0.62	7.55	3.91	7.45	0.56	1.09	3.10	0.68	7.30	15.46	0.00	0.00
Si	45.00	45.00	38.00	58.00	38.00	58.00	65.00	65.00	38.00	38.00	58.00	58.00	65.00	65.00
P	164.60	22.72	6.18	22.78	34.70	44.40	26.48	17.71	44.66	32.19	55.81	32.68	36.67	26.05
Ca	11.18	11.93	0.09	5.22	0.01	4.18	1.33	0.74	0.05	0.02	4.15	2.97	0.35	0.65
Sc	141.53	147.72	9.83	1.24	65.74	0.00	0.83	4.98	86.16	68.50	0.00	3.35	0.00	7.67
V	342.87	332.16	316.80	0.17	263.55	0.70	0.00	0.00	142.91	382.11	2.42	1.48	0.00	0.00
Cr	3.96	8.51	9.79	0.00	43.15	3.27	0.00	4.51	28.78	86.79	3.93	7.78	1.16	2.82
Co	35.04	38.87	44.58	0.00	39.95	0.44	0.00	0.27	23.89	21.99	0.00	0.16	0.07	0.00
Ni	0.68	2.48	7.08	3.10	19.90	1.81	0.22	0.00	12.20	10.89	0.00	2.40	0.00	2.33
Cu	1.13	2.01	1.99	2.73	0.00	5.73	15.42	6.98	12.37	0.00	24.15	27.70	4.95	11.28
Zn	447.47	462.32	398.38	5.96	601.13	7.04	2.86	2.47	733.44	835.03	12.53	15.13	0.69	3.73
Ga	37.61	37.19	76.76	28.57	79.79	30.69	43.94	25.38	92.83	61.89	29.16	26.85	56.93	21.97
Rb	21.33	7.77	806.81	2.22	935.39	1.60	330.36	359.58	1127.63	1069.72	3.45	5.52	372.91	422.23
Sr	22.73	22.82	1.31	358.35	0.28	172.54	103.61	93.93	0.49	0.31	58.34	22.12	71.12	34.14
Y	322.34	315.57	0.13	0.20	0.08	0.79	0.09	0.30	0.21	0.00	2.68	1.45	0.36	0.16
Zr	155.07	158.79	1.54	1.86	10.29	20.39	21.06	8.92	19.46	4.13	18.87	65.05	3.03	17.47
Nb	50.08	53.00	25.13	0.03	139.23	0.10	0.00	0.09	229.20	198.69	2.45	0.50	1.00	0.30
Cs	0.51	0.23	21.02	0.42	27.16	0.08	2.50	1.25	52.46	26.33	1.62	0.80	11.31	2.33
Ba	54.81	38.96	1309.43	99.19	1064.19	110.21	2532.79	419.47	526.49	167.82	36.68	24.59	2955.46	239.46
La	85.69	71.43	0.12	7.06	0.00	9.08	1.39	1.77	0.11	0.00	16.50	1.75	4.03	0.90
Ce	310.93	269.94	0.21	7.90	0.00	12.44	1.39	1.90	0.29	0.06	26.47	3.70	2.98	1.30
Pr	50.12	47.51	0.02	0.46	0.00	0.92	0.00	0.13	0.08	0.02	2.61	0.39	0.08	0.14
Nd	259.43	261.55	0.03	1.89	0.00	3.00	0.57	0.57	0.25	0.06	11.25	1.51	0.20	0.33
Sm	74.68	78.80	0.00	0.20	0.00	0.66	0.00	0.04	0.00	0.00	1.74	0.32	0.04	0.04
Eu	4.57	4.55	0.04	2.37	0.00	1.79	0.79	0.85	0.00	0.02	0.72	0.29	1.27	0.59
Gd	66.27	63.27	0.00	0.20	0.00	0.28	0.00	0.07	0.12	0.00	1.39	0.37	0.03	0.04
Tb	10.76	10.45	0.03	0.02	0.00	0.05	0.00	0.00	0.00	0.00	0.22	0.05	0.00	0.00
Dy	62.01	61.55	0.00	0.00	0.00	0.22	0.00	0.00	0.19	0.00	0.91	0.37	0.00	0.16
Ho	12.14	12.19	0.00	0.00	0.00	0.01	0.00	0.00	0.02	0.02	0.15	0.07	0.00	0.07
Er	29.91	34.62	0.00	0.00	0.00	0.12	0.00	0.00	0.00	0.12	0.48	0.24	0.00	0.20
Tm	4.37	4.50	0.02	0.00	0.00	0.05	0.00	0.00	0.03	0.05	0.06	0.03	0.00	0.04
Yb	25.47	25.02	0.11	0.00	0.00	0.00	0.00	0.00	0.00	0.00	0.31	0.37	0.00	0.26
Lu	3.72	3.92	0.00	0.00	0.00	0.00	0.00	0.00	0.05	0.00	0.06	0.13	0.00	0.03
Hf	9.76	8.62	0.18	0.37	0.91	0.94	0.35	0.43	0.72	0.09	0.15	1.28	0.00	0.44
Ta	2.28	2.39	0.81	0.00	4.58	0.00	0.00	0.00	15.39	5.80	0.10	0.17	0.00	0.00
Tl	0.25	0.00	6.03	0.23	6.90	0.20	1.50	1.92	13.35	9.12	0.09	0.38	1.57	1.95
Pb	7.79	7.76	5.34	15.85	5.64	20.52	290.12	40.01	4.67	4.69	20.03	21.58	44.45	48.89
Th	1.45	0.71	0.00	0.00	0.00	0.00	0.72	0.00	1.85	0.00	0.42	1.80	0.00	7.07
U	0.39	0.26	0.00	0.35	0.00	0.00	0.00	0.17	0.46	0.00	0.00	0.82	0.00	0.00

TABLE III. Whole-rock composition of the Porriño plutonic rocks

Rock type	M. enclave	Gray monzogranite							Pink-red granite				
Sample	GAGR-15	GAGR-6	GAGR-16	GAGR-18	GAGR-14	GAGR-7	GAB-6	GAGR-15-1	GAGR-17	GAGR-5	GAB-8	GAB-12	GAB-7
wt. %													
SiO_2	65.90	69.18	70.57	70.61	70.84	70.87	72.60	72.69	70.71	72.30	72.31	75.91	76.03
TiO_2	0.82	0.37	0.44	0.31	0.38	0.30	0.35	0.20	0.34	0.20	0.28	0.12	0.10
Al_2O_3	14.98	14.84	13.85	14.42	14.02	14.62	13.50	13.70	13.94	13.91	14.39	12.40	12.83
Fe_2O_3	5.27	2.94	3.20	2.48	2.82	2.33	2.34	1.71	3.63	2.11	2.46	1.43	1.38
MnO	0.08	0.04	0.05	0.04	0.04	0.04	0.04	0.03	0.04	0.03	0.05	0.02	0.02
MgO	0.94	0.56	0.60	0.45	0.58	0.41	0.42	0.31	0.37	0.24	0.28	0.06	0.04
CaO	3.00	1.60	2.01	1.32	1.87	1.47	1.29	1.48	1.15	0.92	1.31	0.65	0.67
Na_2O	3.67	3.68	3.61	3.75	3.51	3.90	2.79	3.20	3.63	3.38	3.03	2.55	2.61
K_2O	3.92	5.26	4.08	4.98	4.52	4.98	5.38	5.10	4.65	5.79	5.07	5.49	5.78
P_2O_5	0.26	0.12	0.14	0.10	0.12	0.09	0.10	0.07	0.10	0.05	0.13	0.03	0.03
LOI	0.75	0.57	0.63	0.84	0.71	0.71	0.52	0.60	0.79	0.56	0.38	0.25	0.38
Total	99.60	99.17	99.20	99.32	99.43	99.74	99.33	99.10	99.38	99.48	99.69	98.91	99.87
ppm													
Li	73	91	83	83	74	105	90	33	76	56	92	51	47
Rb	205	293	242	264	240	325	236	208	265	246	203	205	210
Cs	6.3	14.2	10.8	10.9	7.4	10.9	6.9	4.0	9.4	6.9	9.6	5.6	4.3
Be	4.2	6.5	5.1	5.0	4.5	6.8	4.5	3.3	4.1	3.3	3.7	3.1	2.7
Sr	197	89	133	67	117	103	67	169	51	36	67	23	21
Ba	625	383	448	268	455	1342	321	806	317	205	448	156	147
Sc	10	7	8	6	8	7	6	3	9	5	6	4	4
V	51	27	33	19	31	24	22	17	18	8	16	4	4
Cr	13	16	14	10	14	15	13	12	12	11	14	9	9
Co	55	47	59	52	69	51	81	60	57	44	49	52	56
Ni	2	3	3	2	3	3	3	2	2	1	3	1	1
Cu	5	4	3	2	3	3	4	2	2	2	6	2	2
Zn	71	58	72	51	57	56	51	34	89	50	108	43	47
Ga	22.0	24.0	24.0	21.5	24.3	26.4	19.8	17.6	26.6	22.9	19.4	20.1	20.8
Y	36.9	35.0	40.2	42.7	49.9	60.6	39.6	15.9	39.9	26.9	25.1	20.8	20.9
Nb	14.8	15.1	14.7	15.0	16.2	18.9	17.9	5.8	28.0	16.4	15.1	14.4	15.9
Ta	1.8	1.6	1.9	1.9	2.0	2.8	2.0	0.9	1.8	1.1	1.8	1.4	1.1
Zr	193	170	187	118	141	148	204	118	158	143	227	156	163
Hf	5.3	4.2	5.0	3.6	3.9	3.8	5.8	3.1	4.6	3.6	6.2	4.3	4.7
Mo	1.9	0.8	1.0	1.5	2.3	1.3	3.4	0.3	4.1	2.3	2.0	2.1	2.1
Sn	9.3	13.5	9.4	10.2	7.1	10.2	9.3	3.7	8.5	6.0	10.1	4.8	4.1
Pb	23	31	29	30	28	37	31	30	28	29	32	32	33
U	9.2	6.9	9.7	12.1	11.3	17.1	10.2	8.6	7.8	5.1	7.6	7.7	6.6
Th	20.6	25.4	37.5	30.2	32.2	32.5	22.0	17.3	37.7	26.3	15.7	34.6	31.2
La	40.4	38.5	42.8	29.8	41.3	51.5	36.7	25.9	60.9	57.1	34.8	63.3	68.1
Ce	80.7	88.8	90.3	68.9	87.5	84.5	84.4	55.5	144.5	126.6	75.2	130.1	138.8
Pr	9.3	9.6	10.6	8.0	10.4	9.6	9.1	6.1	16.2	14.7	8.7	14.9	15.9
Nd	35.1	35.1	39.3	30.2	38.9	36.5	34.4	21.9	59.5	53.2	33.3	54.7	57.9
Sm	7.2	7.2	8.2	7.2	8.7	9.0	7.5	4.1	12.3	10.1	7.1	10.0	10.8
Eu	1.4	0.7	1.0	0.6	0.9	0.5	0.8	0.8	0.6	0.5	0.9	0.5	0.5
Gd	6.5	6.2	7.3	6.9	8.2	9.0	6.5	3.2	9.6	7.5	5.9	7.3	7.9
Tb	1.0	0.9	1.1	1.1	1.3	1.5	0.9	0.5	1.4	1.0	0.8	0.9	1.0
Dy	6.0	5.5	6.7	7.2	8.2	9.9	5.9	2.6	7.3	5.3	4.6	4.4	4.6
Ho	1.2	1.1	1.3	1.4	1.7	2.0	1.2	0.5	1.4	1.0	0.9	0.8	0.8
Er	3.4	3.2	3.8	4.1	4.6	5.6	3.2	1.5	3.6	2.4	2.2	2.0	1.9
Tm	0.5	0.5	0.6	0.6	0.7	0.9	0.5	0.2	0.5	0.4	0.3	0.3	0.3
Yb	3.5	3.4	3.8	3.9	4.3	5.7	3.2	1.7	3.1	2.1	2.1	1.8	1.7
Lu	0.5	0.6	0.6	0.5	0.6	0.8	0.5	0.3	0.4	0.3	0.3	0.3	0.2

TABLE IV. Summary of SHRIMP U-Pb zircon data for the selected samples of the Porriño pluton

	ppm		Isotope ratios										Ages						
grain	U	Th	$^{206}Pb^*$	% $^{206}Pb_c$	Th/U	$^{207}Pb^*/^{206}Pb^*$	±	$^{206}Pb^*/^{238}U$	±	$^{207}Pb^*/^{235}U$	±	err corr	$^{207}Pb/^{206}Pb$	±	$^{206}Pb/^{238}U$	±	$^{207}Pb/^{235}U$	±	% Disc.
GAB-8: Pink-red granite																			
14.2	795.4	244.3	31.3	0.4	0.32	0.05420	0.00235	0.04544	0.00183	0.33959	0.02016	0.489	379.5	94.8	286.5	11.4	296.9	15.4	3.6
15.1	2716.6	779.1	109.3	0.1	0.29	0.05566	0.00229	0.04636	0.00197	0.35576	0.02108	0.516	438.9	89.2	292.1	12.1	309.0	15.9	5.4
16.1	1398.5	734.2	56.2	0.1	0.54	0.05176	0.00132	0.04637	0.00061	0.33094	0.00959	0.329	274.7	57.6	292.2	3.8	290.3	7.4	-0.6
17.1	587.4	161.7	23.6	-0.2	0.28	0.05132	0.00127	0.04638	0.00063	0.32819	0.00935	0.341	255.3	56.0	292.3	3.9	288.2	7.2	-1.4
19.1	356.0	152.7	14.5	-0.1	0.44	0.05009	0.00140	0.04682	0.00057	0.32336	0.00989	0.285	199.3	63.4	295.0	3.5	284.5	7.6	-3.6
2.1	569.4	56.7	23.1	-0.1	0.10	0.05171	0.00130	0.04686	0.00202	0.33408	0.01675	0.620	272.5	56.6	295.2	12.5	292.7	12.9	-0.8
20.1	2559.2	154.0	104.7	0.0	0.06	0.05213	0.00022	0.04720	0.00070	0.33929	0.00534	0.674	291.3	9.4	297.3	4.3	296.6	4.0	-0.2
20.2	311.3	83.5	12.6	0.2	0.28	0.05171	0.00093	0.04682	0.00073	0.33380	0.00803	0.465	272.5	40.6	295.0	4.5	292.5	6.2	-0.8
21.1	4457.8	387.3	184.1	0.0	0.09	0.05593	0.00039	0.04601	0.00094	0.35481	0.00777	0.671	449.7	15.6	290.0	5.8	308.3	5.8	6.0
23.1	505.1	215.8	20.2	0.1	0.44	0.04967	0.00113	0.04604	0.00061	0.31534	0.00841	0.360	179.9	52.2	290.2	3.8	278.3	6.5	-4.2
26.1	2857.3	198.0	118.8	0.0	0.07	0.05236	0.00024	0.04772	0.00069	0.34447	0.00536	0.667	301.1	10.4	300.5	4.2	300.6	4.1	0.0
28.1	1588.6	300.5	64.6	-0.1	0.19	0.05336	0.00070	0.04701	0.00075	0.34590	0.00725	0.550	344.3	29.2	296.2	4.7	301.6	5.4	1.8
30.1	612.5	213.3	24.5	0.0	0.36	0.05350	0.00135	0.04616	0.00075	0.34049	0.01031	0.388	350.1	56.2	290.9	4.7	297.5	7.8	2.2
31.1	140.2	35.8	5.6	-0.2	0.26	0.05031	0.00155	0.04567	0.00075	0.31676	0.01112	0.337	209.1	70.0	287.9	4.7	279.4	8.6	-3.0
32.1	1455.8	723.3	58.3	-0.1	0.51	0.05256	0.00213	0.04618	0.00083	0.33464	0.01489	0.291	309.7	89.8	291.0	5.1	293.1	11.4	0.8
37.1	180.5	44.0	7.4	0.2	0.25	0.05005	0.00106	0.04738	0.00081	0.32698	0.00897	0.450	197.3	48.2	298.4	5.0	287.3	6.9	-3.8
4.1	2337.5	458.5	96.6	0.0	0.20	0.05191	0.00161	0.04769	0.00202	0.34139	0.01795	0.580	281.7	69.2	300.3	12.4	298.2	13.7	-0.8
9.1	396.7	142.2	16.1	-0.5	0.37	0.05241	0.00270	0.04671	0.00183	0.33755	0.02188	0.436	303.3	113.2	294.3	11.3	295.3	16.7	0.4
Errors are at 95% confidence interval (≈ 2 sigma) . Point to point errors, calculated on replicates of the TEMORA standard at 95% confidence interval, are: 0.13 % for $^{206}Pb/^{238}U$, and 0.35 % for $^{207}Pb/^{206}Pb$.																			
GAGR-5: Pink-red granite																			
11.1	245.4	63.9	9.9	0.6	0.27	0.04897	0.00163	0.04641	0.00053	0.31338	0.01110	0.231	146.7	76.4	292.4	3.2	276.8	8.6	-5.6
12.1	649.7	190.5	25.3	0.1	0.30	0.05026	0.00136	0.04497	0.00091	0.31169	0.01061	0.429	207.3	61.6	283.6	5.6	275.5	8.3	-3.0
16.1	456.3	228.8	18.0	0.1	0.51	0.04922	0.00207	0.04545	0.00058	0.30840	0.01361	0.209	158.1	95.6	286.5	3.6	272.9	10.6	-5.0
17.1	193.7	62.2	7.7	0.3	0.33	0.04917	0.00160	0.04582	0.00044	0.31064	0.01058	0.204	156.1	74.4	288.8	2.7	274.7	8.3	-5.2
18.1	347.7	80.6	13.9	0.2	0.24	0.04916	0.00145	0.04609	0.00054	0.31242	0.01000	0.264	155.7	67.8	290.5	3.4	276.1	7.8	-5.2
19.1	429.0	123.4	17.2	0.1	0.30	0.04962	0.00105	0.04633	0.00066	0.31696	0.00815	0.397	177.3	48.4	291.9	4.0	279.6	6.3	-4.4

Geologica Acta, 15(4), 283-304, I-VII (2017)
DOI: 10.1344/GeologicaActa2017.15.4.3

TABLE IV. (Cont.)

	ppm					Isotope ratios							Ages						
grain	U	Th	$^{206}Pb^*$	% $^{206}Pb_c$	Th/U	$^{207}Pb^*$ /$^{206}Pb^*$	±	$^{206}Pb^*$ /^{238}U	±	$^{207}Pb^*$ /^{235}U	±	err corr	^{207}Pb /^{206}Pb	±	^{206}Pb /^{238}U	±	^{207}Pb /^{235}U	±	% Disc.
20.1	577.2	127.2	22.5	0.2	0.23	0.04935	0.00160	0.04496	0.00063	0.30594	0.01085	0.284	164.3	74.0	283.5	3.9	271.0	8.4	-4.6
22.1	260.7	55.7	10.8	0.0	0.22	0.05142	0.00139	0.04770	0.00058	0.33819	0.01009	0.292	259.7	60.8	300.4	3.6	295.8	7.7	-1.6
23.1	177.9	56.0	7.4	0.8	0.32	0.04874	0.00252	0.04812	0.00063	0.32338	0.01730	0.177	135.1	117.2	303.0	3.9	284.5	13.4	-6.6
24.1	390.1	90.4	15.7	0.2	0.24	0.05174	0.00070	0.04656	0.00038	0.33220	0.00536	0.366	274.1	30.6	293.4	2.4	291.2	4.0	-0.8
25.1	415.4	94.0	16.9	0.3	0.23	0.05184	0.00117	0.04690	0.00050	0.33525	0.00848	0.305	278.3	51.0	295.5	3.1	293.6	6.5	-0.6
26.1	465.3	134.1	18.7	0.2	0.30	0.04869	0.00233	0.04627	0.00122	0.31065	0.01702	0.345	132.9	109.0	291.6	7.5	274.7	13.3	-6.2
27.1	695.1	166.3	28.3	0.2	0.25	0.04920	0.00092	0.04697	0.00050	0.31862	0.00693	0.353	157.1	43.0	295.9	3.1	280.8	5.3	-5.4
28.1	136.7	31.5	5.6	0.5	0.24	0.05082	0.00212	0.04752	0.00066	0.33298	0.01468	0.227	232.7	93.4	299.3	4.1	291.8	11.2	-2.6
29.1	249.2	61.4	10.2	0.3	0.25	0.05167	0.00154	0.04704	0.00058	0.33518	0.01085	0.272	270.9	66.8	296.4	3.6	293.5	8.3	-1.0
30.1	897.7	226.2	36.2	0.1	0.26	0.04912	0.00079	0.04651	0.00047	0.31501	0.00608	0.379	153.7	37.2	293.0	2.9	278.1	4.7	-5.4
32.1	217.5	57.5	9.2	0.4	0.27	0.04915	0.00169	0.04862	0.00038	0.32953	0.01167	0.158	155.1	78.6	306.1	2.4	289.2	8.9	-5.8
4.1	221.5	94.6	8.9	0.6	0.44	0.04689	0.00320	0.04625	0.00081	0.29898	0.02111	0.178	0.0	199.3	291.4	5.0	265.6	16.6	-9.8
5.1	151.9	37.6	5.8	0.6	0.25	0.05271	0.00153	0.04431	0.00058	0.32199	0.01032	0.293	316.3	64.8	279.5	3.6	283.4	7.9	1.4
6.2	356.6	81.1	13.9	0.4	0.23	0.04700	0.00125	0.04490	0.00061	0.29101	0.00874	0.324	0.0	111.7	283.1	3.7	259.4	6.9	-9.2
7.1	306.5	99.5	12.4	0.3	0.33	0.04803	0.00255	0.04668	0.00127	0.30913	0.01850	0.329	100.9	121.0	294.1	7.9	273.5	14.4	-7.6
8.1	157.7	42.4	6.5	0.7	0.28	0.04636	0.00263	0.04763	0.00054	0.30442	0.01764	0.142	0.0	147.1	299.9	3.3	269.8	13.8	-11.2
Errors are at one sigma level. The error in 206/238 averaging the standard has been already propagated. Point to point errors, calculated on replicates of the TEMORA standard, are: 0.62 % for $^{206}Pb/^{238}U$, and 0.61 % for $^{207}Pb/^{206}Pb$.																			
GAB-6: Gray monzogranite																			
1.1	88.1	20.6	3.8	0.1	0.24	0.03231	0.00893	0.04625	0.00109	0.20603	0.05715	0.061	0.0	98.9	291.5	6.7	190.2	49.3	-53.2
1.2*	161.9	53.4	6.4	0.0	0.34	0.01147	0.00637	0.03614	0.00114	0.05715	0.03179	0.041	0.0	98.9	228.8	7.0	56.4	31.0	-305.6
13.1	2381.3	430.7	98.0	0.1	0.19	0.05219	0.00047	0.04755	0.00063	0.34219	0.00563	0.580	293.7	20.6	299.5	3.9	298.8	4.2	-0.2
14.1*	779.5	275.2	36.4	12.3	0.36	0.05578	0.00785	0.04745	0.00068	0.36495	0.05162	0.073	443.9	285.6	298.8	4.2	315.9	39.1	5.4
15.2	1033.8	141.6	42.7	0.6	0.14	0.05284	0.00035	0.04759	0.00038	0.34672	0.00382	0.524	322.1	15.0	299.7	2.4	302.2	2.8	0.8
16.1	3381.2	691.1	147.2	1.1	0.21	0.05123	0.00062	0.04876	0.00072	0.34442	0.00673	0.546	251.1	27.8	306.9	4.4	300.5	5.1	-2.2
17.1	2020.6	309.5	80.3	2.3	0.16	0.04736	0.00059	0.04464	0.00048	0.29152	0.00491	0.457	67.5	29.4	281.5	2.9	259.8	3.9	-8.4
18.1	3148.4	544.1	124.1	1.8	0.18	0.05138	0.00235	0.04418	0.00081	0.31305	0.01545	0.268	258.1	101.6	278.7	5.0	276.5	12.0	-0.8

Geologica Acta, 15(4), 283-304, I-VII (2017)
DOI: 10.1344/GeologicaActa2017.15.4.3

TABLE IV. (Cont.)

	ppm		Isotope ratios										Ages						
grain	U	Th	$^{206}Pb^*$	% $^{206}Pb_c$	Th/U	$^{207}Pb^*$ /$^{206}Pb^*$	±	$^{206}Pb^*$ /^{238}U	±	$^{207}Pb^*$ /^{235}U	±	err corr	^{207}Pb /^{206}Pb	±	^{206}Pb /^{238}U	±	^{207}Pb /^{235}U	±	% Disc.
2.1	180.8	38.3	7.5	0.1	0.22	0.05313	0.00097	0.04795	0.00111	0.35124	0.01046	0.561	334.5	41.0	301.9	6.9	305.7	7.9	1.2
2.2*	73.6	20.1	3.0	0.0	0.28	0.04267	0.00185	0.04621	0.00091	0.27188	0.01298	0.298	0.0	81.7	291.2	5.6	244.2	10.4	-19.2
20.1	719.4	235.3	79.5	8.1	0.34	-0.16680	0.00169	0.08493	0.00136	-1.95331	-0.03757	0.598	0.0	98.9	525.5	8.1	.	.	.
21.1	2967.4	818.4	122.4	0.0	0.28	0.05376	0.00102	0.04725	0.00090	0.35024	0.00951	0.504	360.9	42.4	297.6	5.5	304.9	7.2	2.4
23.1	4653.0	365.7	195.9	0.4	0.08	0.05176	0.00131	0.04638	0.00098	0.33098	0.01100	0.458	274.9	57.0	292.2	6.0	290.3	8.4	-0.6
26.1*	1693.5	987.1	88.5	8.0	0.60	0.04293	0.00457	0.04499	0.00162	0.26626	0.02997	0.231	0.0	74.5	283.7	10.1	239.7	24.3	-18.4
27.2*	856.7	243.7	36.9	3.5	0.29	0.02639	0.00244	0.04247	0.00163	0.15452	0.01550	0.276	0.0	98.9	268.1	10.1	145.9	13.7	-83.8
3.1	253.9	33.3	10.6	0.0	0.13	0.05190	0.00079	0.04818	0.00119	0.34476	0.01008	0.610	281.1	34.2	303.3	7.3	300.8	7.7	-0.8
3.2*	51.4	22.4	2.0	0.1	0.45	0.04223	0.00351	0.04300	0.00149	0.25037	0.02254	0.277	0.0	16.3	271.4	9.2	226.9	18.5	-19.6
30.1*	2854.3	627.7	119.6	3.2	0.23	0.03454	0.01214	0.04526	0.00190	0.21557	0.07628	0.085	0.0	32.9	285.4	11.8	198.2	65.8	-44.0
32.1	2704.3	407.8	108.0	0.0	0.15	0.04957	0.00127	0.04584	0.00203	0.31329	0.01605	0.622	174.7	58.6	288.9	12.5	276.7	12.5	-4.4
32.2*	1556.5	267.9	75.6	6.0	0.18	0.00210	0.00514	0.04585	0.00184	0.01328	0.03250	0.012	0.0	98.9	289.0	11.3	13.4	33.1	-2056.8
33.1*	1838.2	285.3	82.5	4.0	0.16	0.04789	0.01833	0.04662	0.00211	0.30784	0.11866	0.084	93.9	719.6	293.7	13.0	272.5	96.6	-7.8
33.2*	624.8	228.5	26.9	3.7	0.38	0.04942	0.00393	0.04612	0.00221	0.31422	0.02920	0.371	167.7	176.0	290.6	13.6	277.4	22.8	-4.8
33.3*	1344.8	212.0	57.8	2.0	0.16	0.04865	0.00136	0.04723	0.00183	0.31687	0.01519	0.583	131.3	64.2	297.5	11.3	279.5	11.8	-6.4
34.1	3197.3	689.0	129.2	0.0	0.22	0.04236	0.00187	0.04548	0.00190	0.26565	0.01617	0.494	0.0	97.7	286.7	11.7	239.2	13.1	-19.8
36.1	4633.1	882.9	204.8	0.5	0.20	0.05059	0.00178	0.04845	0.00200	0.33791	0.01838	0.548	221.9	79.4	305.0	12.4	295.6	14.1	-3.2
36.1*	1554.8	461.1	63.6	0.3	0.30	0.05005	0.00243	0.04671	0.00201	0.32232	0.02096	0.477	197.3	109.2	294.3	12.4	283.7	16.2	-3.8
37.1	6002.4	1703.3	269.6	0.6	0.29	0.05119	0.00219	0.04782	0.00204	0.33752	0.02044	0.508	249.5	95.4	301.1	12.6	295.3	15.6	-2.0
5.1	53.8	15.1	2.1	0.1	0.29	0.05215	0.00123	0.04556	0.00097	0.32754	0.01047	0.479	291.9	52.8	287.2	6.0	287.7	8.1	0.2
6.1*	3357.7	653.6	137.2	0.1	0.20	0.05251	0.00151	0.04640	0.00193	0.33594	0.01704	0.590	307.7	64.4	292.4	11.9	294.1	13.0	0.6
6.2	528.1	156.1	21.2	0.0	0.30	0.05153	0.00220	0.04644	0.00177	0.33000	0.01892	0.479	264.7	95.2	292.6	10.9	289.6	14.6	-1.0
7.1	1693.6	194.8	66.5	0.1	0.12	0.04716	0.00091	0.04508	0.00186	0.29314	0.01341	0.651	57.7	45.2	284.2	11.5	261.0	10.6	-8.8
8.1	1157.0	307.9	42.9	0.1	0.27	0.05133	0.00219	0.04273	0.00187	0.30241	0.01850	0.514	255.7	95.4	269.7	11.5	268.3	14.5	-0.6
9.1	5144.4	471.0	217.8	0.3	0.09	0.05206	0.00088	0.04617	0.00209	0.33142	0.01608	0.672	287.9	38.4	291.0	12.9	290.6	12.3	-0.2

(*) used only for discordia line.
Errors are at 95% confidence interval (≈ 2 sigma)
Point to point errors, calculated on replicates of the TEMORA standard, are: 0.38 % for $^{206}Pb/^{238}U$, and 0.46 % for $^{207}Pb/^{206}Pb$.

Geologica Acta, 15(4), 283-304, I-VII (2017)
DOI: 10.1344/GeologicaActa2017.15.4.3

TABLE IV. (Cont.)

	ppm					Isotope ratios							Ages						
grain	U	Th	$^{206}Pb^*$	% $^{206}Pb_c$	Th/U	$^{207}Pb^*/^{206}Pb^*$	±	$^{206}Pb^*/^{238}U$	±	$^{207}Pb^*/^{235}U$	±	err corr	$^{207}Pb/^{206}Pb$	±	$^{206}Pb/^{238}U$	±	$^{207}Pb/^{235}U$	±	% Disc.
GAGR-16: Gray monzogranite																			
10.2	821.0	161.7	33.6	0.9	0.20	0.04905	0.00076	0.04677	0.00047	0.31631	0.00595	0.381	150.5	36.0	294.6	2.8	279.1	4.6	-5.6
14.1	2504.1	219.5	99.5	0.0	0.09	0.05158	0.00035	0.04587	0.00009	0.32617	0.00260	0.185	266.7	15.6	289.1	0.6	286.6	2.0	-0.8
14.2	577.0	111.7	21.9	0.0	0.20	0.05421	0.00097	0.04395	0.00021	0.32847	0.00621	0.183	379.7	39.8	277.3	1.3	288.4	4.8	3.8
17.1	3383.6	478.7	132.6	0.6	0.15	0.04799	0.00058	0.04473	0.00042	0.29602	0.00467	0.431	98.9	28.4	282.1	2.6	263.3	3.7	-7.2
23.2	914.3	299.6	35.5	0.6	0.34	0.04908	0.00160	0.04448	0.00064	0.30100	0.01077	0.290	151.5	74.6	280.5	3.9	267.2	8.5	-5.0
24.1	617.4	316.6	24.9	0.0	0.53	0.05072	0.00270	0.04652	0.00030	0.32532	0.01746	0.085	228.1	118.4	293.1	1.8	286.0	13.5	-2.4
27.1	1975.1	315.3	77.4	0.2	0.16	0.05105	0.00083	0.04523	0.00021	0.31837	0.00552	0.193	242.9	37.2	285.2	1.3	280.7	4.3	-1.6
28.1	1215.9	236.7	47.9	0.0	0.20	0.05202	0.00072	0.04554	0.00029	0.32664	0.00512	0.297	286.5	31.2	287.1	1.9	287.0	3.9	0.0
29.1	4294.8	1044.0	176.5	0.1	0.25	0.05202	0.00050	0.04751	0.00024	0.34073	0.00389	0.323	286.3	21.6	299.2	1.5	297.7	2.9	-0.6
32.1	410.3	142.1	16.5	0.0	0.36	0.05239	0.00125	0.04632	0.00030	0.33462	0.00836	0.188	302.7	53.4	291.9	1.9	293.1	6.4	0.4
36.1	1453.7	561.7	58.0	0.4	0.40	0.04958	0.00100	0.04574	0.00042	0.31269	0.00704	0.295	175.1	46.6	288.3	2.6	276.3	5.5	-4.4
4.1	7019.3	694.4	301.0	0.4	0.10	0.05141	0.00056	0.04934	0.00022	0.34973	0.00429	0.259	259.3	24.8	310.5	1.4	304.5	3.2	-2.0
7.1	5425.9	1063.5	217.7	0.4	0.20	0.05023	0.00209	0.04606	0.00126	0.31900	0.01594	0.394	205.5	94.0	290.3	7.8	281.1	12.3	-3.2

Errors are at 95% confidence interval (≈ 2 sigma)
Point to point errors, calculated on replicates of the TEMORA standard at 95% confidence interval, are: 0.39 % for $^{206}Pb/^{238}U$, and 0.79 % for $^{207}Pb/^{206}Pb$.

Th/U ratios are atomic (232/238), not in weight. Pbc and Pb*indicate the common and radiogenic portions, respectively. Common Pb corrected using measured ^{204}Pb.

TABLE V. Sr and Nd isotope composition data of the Porriño plutonic rocks

	Rb (ppm)	Sr (ppm)	$^{87}Rb/^{86}Sr$	$^{87}Sr/^{86}Sr$	2σ error	$(^{87}Sr/^{86}Sr)i$	Sm (ppm)	Nd (ppm)	$^{147}Sm/^{144}Nd$	$^{143}Nd/^{144}Nd$	2σ error	$(^{143}Nd/^{144}Nd)i$	ε(Nd)t	T_{CHUR} (Ma)	T_{CR} (Ma)	T_{DM} (Ma)
Pink- red granite																
GAB-7	209.67	21.35	28.733100	0.824757	0.002	0.704142	10.30	56.73	0.110	0.512429	0.003	0.512221	-0.86	367	1064	905
GAB-12	204.54	23.04	25.941128	0.810758	0.008	0.701863	10.07	56.71	0.107	0.512389	0.003	0.512185	-1.55	426	1097	940
GAB-8	202.95	67.12	8.780938	0.747088	0.008	0.710228	7.23	33.31	0.131	0.512458	0.002	0.512209	-1.09	420	1286	1080
Gray monzogranite																
GAB-6	235.99	67.68	10.127161	0.747674	0.002	0.705162	7.79	35.26	0.134	0.512491	0.002	0.512237	-0.53	356	1261	1050
GAGR-14	239.70	117.07	5.936560	0.730550	0.003	0.705630	8.69	38.88	0.135	0.512492	0.002	0.512236	-0.57	362	1283	1068
Mafic Enclave																
GAGR-15	170.83	192.37	2.571421	0.717384	0.003	0.706590	6.74	31.93	0.128	0.512441	0.002	0.512199	-1.28	435	1261	1065

Geologica Acta, 15(4), 283-304, I-VII (2017)
DOI: 10.1344/GeologicaActa2017.15.4.3